Carbon Letters (2024) 34:227–245
https://doi.org/10.1007/s42823-023-00634-9

Online ISSN 2233-4998
Print ISSN 1976-4251

REVIEW

2D/2D composites based on graphitic carbon nitride and MXenes for photocatalytic reactions: a critical review

Petr Praus[1,2]

Received: 11 July 2023 / Revised: 15 October 2023 / Accepted: 23 October 2023 / Published online: 11 November 2023

Abstract

The combination of the two-dimensional (2D) materials g-C_3N_4 and MXenes in photocatalysis offers several advantages. The g-C_3N_4 can serve as a visible light-absorbing material, while MXenes can enhance the charge separation and transfer processes leading to improved photocatalytic efficiency. A critical review of 77 already published articles in the field of photocatalytic reactions using g-C_3N_4 and MXenes, such as hydrogen evolution, the reduction of carbon dioxide, the degradation of organic compounds, the redox reactions of nitrogen, was conducted. For the purpose of greater objectivity, the published results were analysed by non-parametric Mann–Whitney, Kolmogorov–Smirnov, and Mood´s median tests and visualised by box and whisker plots. It was found that MXenes can significantly improve the photocatalytic activity of g-C_3N_4. Adding other co-catalysts to the MXene/g-C_3N_4 composites does not bring a significant improvement in the photocatalytic performance. Promising results were obtained especially in the fields of hydrogen evolution and the reduction of carbon dioxide. Since the MXenes are relatively a new class of materials, there is still a big challenge for finding new photocatalytic applications and for the enhancement of existing photocatalytic systems based on g-C_3N_4, especially in terms of the MXenes and g-C_3N_4 surface and in the heterojunction engineering.

Keywords g-C_3N_4 · MXene · Photocatalysis

1 Introduction

Graphitic carbon nitride is a metal free polymeric semiconductor (a band gap energy of 2.7 eV) which has been intensively studied since 2009 when Wang et al. published their paper about water splitting using g-C_3N_4 [1]. It has noteworthy physico-chemical properties, such as high thermal, physical, chemical, and photochemical stability. There properties were reviewed in many comprehensive papers, for example, [2–10].

MXenes are a novel group of materials which have been studied since a paper of Naguib and co-authors was published in 2011 [11]. MXenes are formed by the etching of MAX phases, where M is metal (Ti, V, Nb, Ta, Mo etc.), A is III or IV element and X is carbon and/or nitrogen, forming materials with a general formula of $M_{n+1}X_nT_x$ (n = 1–4), where T is a surface functional group, such as O, OH, and F. MXenes are important materials due to their high, conductivity and specific surface area, thermal and mechanical stability, hydrophilicity, and tuneable surface chemistry. The various MXene properties and possible applications were reviewed in the literature, for example, [12–19].

The combination of g-C_3N_4 and MXenes for photocatalysis began to be interesting for scientists since 2017 when Shao et al. [20] referred to the hydrogen evolution reaction (HER) in the presence of these materials. Both g-C_3N_4 and MXenes are 2D materials and their benefits are the following: (1) the absorption of light can be controlled by their thickness, (2) the migration path of charge carries to the surface is short, and (3) these materials have a high surface area and provide a lot of active sites for redox reactions [21]. In addition, composite 2D/2D materials have a high coupling interface which can accelerate the charge migration at their interface.

✉ Petr Praus
petr.praus@vsb.cz

[1] Department of Chemistry and Physico-Chemical Processes, Faculty of Materials Science and Technology, VSB-Technical University of Ostrava, 17. Listopadu 15, 708 00 Ostrava-Poruba, Czech Republic

[2] Institute of Environmental Technology, CEET, VSB-Technical University of Ostrava, 17. Listopadu 15, 708 00 Ostrava-Poruba, Czech Republic

On the whole, the combination of g-C_3N_4 and MXenes in photocatalysis offers several advantages. G-C_3N_4 can serve as a visible light-absorbing material generating photoinduced electrons and holes, while MXenes can enhance the charge separation and its transfer processes, leading to improved photocatalytic efficiency. The large surface area of MXenes provides abundant active sites for catalytic reactions, further enhancing the overall performance of the photocatalytic system.

The aim of this review is to summarize the already published photocatalytic applications of the g-C_3N_4 and MXenes composites and to critically assess the synergy of both materials and their suitability for various reactions. For this purpose, the non-parametric Mann–Whitney and Kolmogorov–Smirnov, and Mood's median tests [22] were used. The reaction data were visualised by box and whisker plots.

2 A review of literature data

Peer reviewed research articles reporting the photocatalytic application of the g-C_3N_4 and MXene composites were mostly taken from journals indexed in the Web of Science. In total, only 77 articles containing results suitable for the statistical assessment were used in this study. In fact, more articles have been published so far but they did not contain the necessary reaction data. The non-parametric Mann–Whitney, Kolmogorov–Smirnov, and Mood's median tests, without making any assumptions of the statistical distributions, were used for this purpose. A hypothesis, if there is a significant difference in the distributions of two data groups, was tested at a significance level $\alpha = 0.05$ (OriginPro 2018, OriginLab Corporation, Norhamptnon, MA, USA). In Fig. 1, it is visible that the g-C_3N_4 and MXene composites were mostly applied for the photocatalytic degradation of organic compounds (31%) and the hydrogen evolution (30%). A smaller part about 19% was devoted to the reduction of carbon dioxide. The rest of the applications was devoted to the nitrogen redox reactions and other ones.

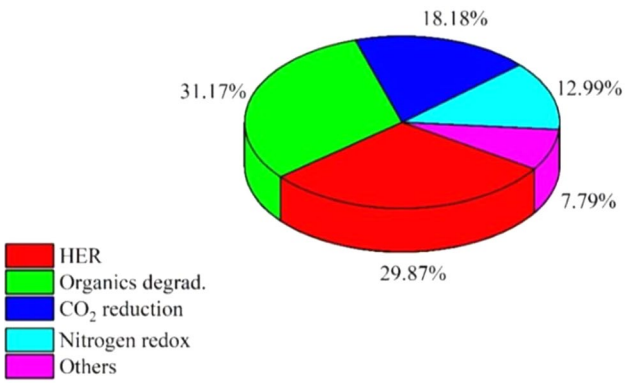

Fig. 1 An overview of the works published on the g-C_3N_4 and MXene composites for various photocatalytic reactions

3 Hydrogen evolution reaction

It is widely accepted, e.g. [23], that the catalytic hydrogen evolution mechanism consists of several steps in acidic conditions

$$H_3O^+ + e^- + C \rightarrow C{-}H + H_2O \quad \text{(Volmer)} \tag{1}$$

$$C{-}H + H_3O^+ + e^- \rightarrow H_2 + H_2O + C \quad \text{(Heyrovský)} \tag{2}$$

$$2\,C{-}H \rightarrow 2\,C + H_2 \quad \text{(Tafel)} \tag{3}$$

and in alkaline conditions

$$H_2O + e^- + C \rightarrow C{-}H + OH{-} \quad \text{(Volmer)} \tag{4}$$

$$H_2O + e^- + C{-}H \rightarrow H_2 + OH{-} \quad \text{(Heyrovský)} \tag{5}$$

where C refers to a vacant surface site on a catalyst and C–H means an adsorbed hydrogen atom on the catalyst.

The first paper on the application of the composite g-C_3N_4 and Ti_2C for the hydrogen evolution by water splitting was published in 2017 by Shao et al. [20]. For this purpose, a standard AM 1.5 solar simulator was used. The highest production of hydrogen of 47.5 μmol h^{-1} (recalculated at 950 μmol h^{-1} g^{-1}) was reached using a Ti_2C loading of 0.4 wt%. Moreover, Ti_2C itself also showed the evolution of hydrogen because it formed TiO_2 and Ti_2CO_2. The production of bare g-C_3N_4 was 66.0 μmol h^{-1} g^{-1}. The apparent quantum efficiency (AQE) was 4.3%. Triethanolamine (TEOA) was used as a hole scavenger.

The Ti_3C_2 MXene and a Pt co-catalyst in combination with g-C_3N_4 were used for HER by An et al. in 2018 [24]. The hydrogen production of 5.1 mmol h^{-1} g^{-1} was achieved under the irradiation of a 300 W xenon lamp. The AQE was about 3.1% at 420 nm. A synergy effect of Ti_3C_2 and Pt nanoclusters was ascribed to the efficient separation of the photoinduced electrons and holes. It was found that more -O surface terminations improve the HER performance. The holes were scavenged by TEOA.

The composite of g-C_3N_4 and Ti_3C_2 with oxygen terminating surface groups was prepared by Sun et al. [25]. The best hydrogen production performance reached 88 μmol h^{-1} g^{-1} and the AQE was 1.27% (using TEOA). DFT calculations demonstrated that the oxygen terminations were covered by hydrogen atoms.

Zhang et al. [26] mixed delaminated Ti_3C_2 with the nanosheets of g-C_3N_4 and calcinated these mixture at 350 °C for 1 h to obtain a Ti_3C_2/TiO_2/g-C_3N_4 composite.

The composite was used for HER under an Xe lamp with a 420 nm cut-off filter. The hydrogen production reached 1.62 mmol h^{-1} g^{-1} and the AQE was 4.16% at 420 nm (with TEOA).

Hexagonal Ni_3C nanoparticles were coupled with g-C_3N_4 by a simple grinding method [27]. A resulting nanocomposite containing 15 wt% Ni_3C produced 304 µmol h^{-1} g^{-1} corresponding to the AQE of 0.40% at 420 nm. The Xe arc lamp (350 W) with an UV cut-off filter (> 420 nm) was used as a source of irradiation.

Ti_3C_2 quantum dots from Ti_3AlC_2 powders were synthetized by Li et al. [28]. The quantum dots in combination with g-C_3N_4 reached the hydrogen production rate of 5111.8 µmol g^{-1} h^{-1} which is 26 times higher than that of bare g-C_3N_4 (196.8 µmol h^{-1} g^{-1}). The highest AQE was 3.654% under simulated solar irradiation produced by a 300 W Xe arc lamp equipped with an AM-1.5 filter.

The synthesis of Ti_3C_2 and O-doped g-C_3N_4 composites was reported by Lin et al. [29]. The composite Ti_3C_2/O-doped g-C_3N_4 (see Fig. 2) produced hydrogen at the rate of 25,124 µmol g^{-1} h^{-1} in comparison to 13,745 µmol g^{-1} h^{-1} and 15,573 µmol g^{-1} h^{-1} provided by single O-doped g-C_3N_4 and Ti_3C2/g-C_3N4, respectively. The AQE values were measured at 17.59% and 6.53% for 405 nm and 420 nm, respectively (with TEOA). The Schottky junction between the MXene and graphitic carbon nitride was based on their electrostatic assembly and resulted in a short charge transport distance from g-C_3N_4 and Ti_3C_2. Oxygen doping was found to improve the separation of the electrons and holes.

The synthesis of Ti_3C_2/g-C_3N_4 composites based on their electrostatic self-assembly was also described by Su et al. [30]. Ti_3C_2 was found to be -O terminated. The optimized composite reached the hydrogen performance of 72.3 µmol g^{-1} h^{-1} (using TEOA) under a Hg lamp equipped with a cut-off filter for 400 nm.

The Ti_3C_2/g-C_3N_4 composites were prepared by the mechanical mixing of sonicated g-C_3N_4 and plasma treated Ti_3C_2. Hydrogen was evolved with the maximum rate of 17.8 µmol h^{-1} g^{-1} under a 350 W Xe arc lamp (a cut-off filter for 400 nm, TEOA) [31]. The improved photocatalytic activity was explained by the presence of Ti^{4+} due to the plasma treatment, which could capture photo-induced electrons from g-C_3N_4 and thus improved their separation from the holes. The plasma treatment modified the surface functional groups of Ti_3C_2, and the increase of Ti–O and the reduction of Ti–C, Ti–F and Ti–OH were observed. Bare g-C_3N_4 provided only 0.7 µmol h^{-1} g^{-1} of hydrogen.

In the work of Han et al. [32] the MXene Ti_3C_2 served for the synthesis of C-TiO_2/g-C_3N_4 by the heating of a mixture of Ti_3C_2 and g-C_3N_4 at 450 °C for 4 h. In fact, Ti_3C_2 was designed of C-doped TiO_2, forming a C-TiO_2/g-C_3N_4 photocatalyst. The hydrogen production rate was 1409 µmol h^{-1} g^{-1}. The production using g-C_3N_4 was 174 µmol h^{-1} g^{-1} using TEOA for scavenging the holes.

Zhang et al. [33] synthesized rod-like g-C_3N_4 decorated by Mo_2C for the hydrogen evolution. The highest rate of 507 µmol h^{-1} g^{-1} was reached with an AQE of 3.74% (420 nm) using TEOA. The decorating Mo_2C co-catalysts on the surface of g-C_3N_4 led to an improved visible light absorption and promoted charge separation.

The 3D hollow spheres of Ti_3C_2 and g-C_3N_4 were synthetized by Kang et al. [34]. A 2D heterostructure shortened the electron migration distance and formed the Schottky

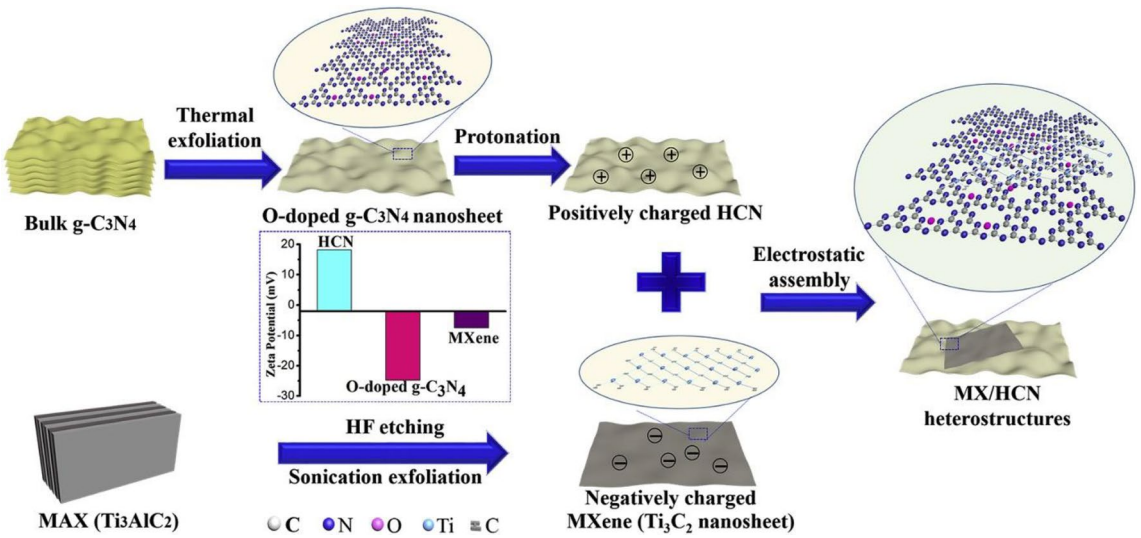

Fig. 2 The synthetic process of the 2D/2D Ti_3C_2/O–g-C_3N_4 Schottky-junction. Reproduced from Ref. [29]. Copyright (2019), with permission from Elsevier

junction to facilitate the separation and transfer of the charge carriers. The hydrogen production rate of the hollow spheres was 982.8 μmol h^{-1} g^{-1} while that of g-C_3N_4 was 1279.5 μmol h^{-1} g^{-1} using TEOA.

The in-situ fabrication of the 2D/3D g-C_3N_4/Ti_3C_2 heterojunction as the Schottky catalyst was referred by Li et al. [35]. A hydrogen evolution rate of 116.2 μmol h^{-1} g^{-1} (using TEOA) was reported. Using pure g-C_3N_4 the rate was 17.5 μmol h^{-1} g^{-1}. The MXene -F termination was removed or replaced by terminal -O during the synthetic process. The experimental and theoretical studies confirmed that the ability of conductive Ti_3C_2 greatly restrained the electron–hole recombination on the g-C_3N_4 and numerous functional groups on the surface of Ti_3C_2 provided sufficient active sites for the HER.

Dong et al. [36] synthesised the 2D/2D g-C_3N_4/Ti_3C_2 composites providing the hydrogen evolution rate of 534 μmol h^{-1} g^{-1} in comparison with g-C_3N_4 providing the rate of 250 μmol h^{-1} g^{-1}. The AQE was 1.61% using a 300 W Xe arc lamp equipped with a cut-off filter ($\lambda > 420$ nm, 150 mW cm^{-2}). TEOA was used as the scavenger.

A 2D/2D/2D Bi_2WO_6/g-C_3N_4/Ti_3C_2 composite was synthetized by a one-step method [37]. The highest rate of 54.4 μmol h^{-1} g^{-1} was reached under a 300 W Xenon lamp and with a TEOA scavenger. The AQE was 1.6% at 420 nm. Ti_3C_2 was found not only to accelerate a Z-scheme charge transfer but also enhance the visible light absorption and redox ability of the Bi_2WO_6/g-C_3N_4 composite.

Crystalline carbon nitride was anchored on Ti_3C_2 as the ordered Schottky heterojunction photocatalyst for the enhanced visible-light hydrogen evolution [38]. Under the irradiation of 420 nm the hydrogen evolution rate was 4225 μmol h^{-1} g^{-1} and the AQE was 14.6% (TEOA). For comparison, the hydrogen rate in the presence of g-C_3N_4 was 513 μmol h^{-1} g^{-1}. The photocatalytic enhancement was attributed to the synergistic effects of the crystallization of g-C_3N_4, the high conductivity of Ti_3C_2 and the well-constructed Schottky heterojunction.

An ultrathin Ti_3C_2 was applied to accelerate the charge transfer in an ultrathin metal-free 0D/2D black phosphorus/g-C_3N_4 heterojunction for the hydrogen production [39]. The optimized composites exhibited the production rate of 18,420 μmol h^{-1} g^{-1} which was 47.2 times more than that of bare g-C_3N_4. The irradiation was produced by a 300 W Xe lamp equipped with a 420 nm cut-off filter.

The Schottky heterojunction of protonated g-C_3N_4 and Ti_3C_2 was constructed by Xu et al. [40]. Strong interfacial interactions highly improved the hydrogen evolution rate at 2181 μmol h^{-1} g^{-1} in comparison with bare g-C_3N_4 (393 μmol h^{-1} g^{-1}) and protonated g-C_3N_4 (816 μmol h^{-1} g^{-1}). The charge-regulated surfaces and the accelerated charge transport over the 2D/2D Schottky heterojunction interface are the main reasons for the higher hydrogen evolution performance of the composite photocatalyst. The AQE at 420 nm was 8.6%. Isopropanol was used as the scavenger.

Hieu et al. [41] synthetized ternary TiO_2/Ti_3C_2/g-C_3N_4 heterojunction photocatalysts for the hydrogen evolution. The ternary composite was prepared by the annealing of Ti_3C_2/g-C_3N_4 in the air at 550 °C for 4 h. The highest evolution rate reached 1150 μmol h^{-1} g^{-1} while bare g-C_3N_4 provided 150 μmol h^{-1} g^{-1} (TEOA was used as the scavenger).

2D/2D Mo_2C/g-C_3N_4 composites were prepared by Liu et al. [42]. The hydrogen production rate of the photocatalyst at the optimal ratio was 675.27 μmol g^{-1} h^{-1}. The enhanced photocatalytic activity was explained so that Mo_2C can rapidly transfer photoinduced electrons from g-C_3N_4 to its surface and thus prevent their recombination with the holes.

3D interconnected g-C_3N_4 hybridized with 2D Ti_3C_2 MXene nanosheets were synthetized by Liu et al. [43]. The MXene termination by –F and –O was identified. This provided a more negative Fermi level than g-C_3N_4 (about − 0.22 V) which is favourable for the electrons to migrate to Ti_3C_2. The HER performance of the composite was 1948 μmol h^{-1} g^{-1} compared with 118.1 μmol h^{-1} g^{-1} of pure g-C_3N_4 (with TEOA). The AQE at 420 nm was determined at 3.83%. The high specific surface area (85 m^2 g^{-1}) and highly efficient charge migration led to the improved hydrogen generation.

In the work of Huang et al. [44], Pt nanoparticles were employed to modify few-layer Ti_3C_2 sheets which were further used as efficient co-catalysts to enhance the photocatalytic hydrogen evolution of g-C_3N_4. The Ti–O bonds were observed on the MXene surface. Using several sacrificial agents, such as methanol, TEOA, lactic acid, and Na_2S/Na_2SO_3, the maximal HER performance of 2644 μmol h^{-1} g^{-1} was achieved in the case of a 5% composite of Pt (with Na_2S/Na_2SO_3). The AQE values at 365 nm and 420 nm were 12.9% and 8.3%, respectively. When methanol was used the HER performance of 2308 μmol h^{-1} g^{-1} and 243 μmol h^{-1} g^{-1} were observed for the 5% Pt composites.

Phosphorus-doped g-C_3N_4 and Ti_3C_2 composites were tested for the HER [45] as well. The presence of –O terminations and TiO_2 was found. The highest achieved performance under the 300 W Xe lamp was 565 μmol h^{-1} g^{-1} in comparison with 107 μmol h^{-1} g^{-1} of g-C_3N_4 and 184 μmol h^{-1} g^{-1} of P-doped g-C_3N_4. The AQE at 420 nm was 5.9%. Methanol was used as the scavenger.

3.1 The quantum efficiency of HER

Quantum efficiency is an important factor of the photocatalytic HER. However, only little information is available in the literature. Only 15 articles reported these data. The basic summary is given in Table 1 where the quantum efficiency was expressed as the AQE. Since the AQE strongly

Table 1 AQE at 420 nm of all kinds of MXene and g-C_3N_4 composites

Statistics	AQE (%)	Statistics	AQE (%)
Number	15	Median	3.83
Minimum	0.4	3rd Quartile	6.22
Maximum	14.6	Mean	4.77
1st quartile	2.36	Standard deviation	3.65

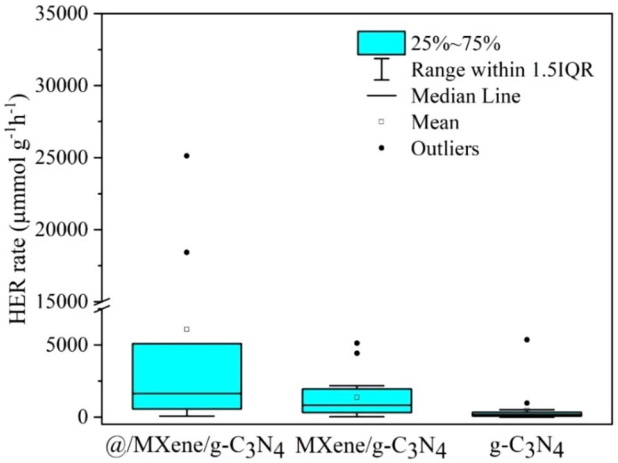

Fig. 3 Box plots of the HER rate of @/MXene/g-C_3N_4 (left), MXene/g-C_3N_4 (centre), and g-C_3N_4 (right)

depends on the irradiation wavelength, only those measured at 420 nm are given here. Their values varied from 0.4 to 14.6%.

3.2 The performance of HER

All the above-mentioned articles are summarized in Table S1. When comparing the results of the photocatalytic reactions, it is possible to take into account that the same kinds of reactions (HER) were performed under different experimental conditions, such as the types of reactors and their geometry, the positions of the irradiation sources, irradiation intensity, photocatalyst concentrations, reaction temperatures, etc. These different experimental conditions can be visible when the photocatalytic rates obtained using the same photocatalyst, that is bare g-C_3N_4, are compared. The HER rates were visualised by the box and whisker lots as shown in Fig. 3.

The composites of MXene, g-C_3N_4 and other co-catalysts were labelled as @/MXene/g-C_3N_4. It is clearly visible that two HER rates are outlying. The basic descriptive statistics are given in Table S2.

The highest (outlying) HER rate of 25,124 μmol h^{-1} g^{-1} and 5366 μmol h^{-1} g^{-1} corresponding to the Ti_3C_2 and O-doped g-C_3N_4 composite and g-C_3N_4, respectively were obtained by Lin et al. [29]. The next very high HER rates of 18,420 μmol h^{-1} g^{-1} and 950 μmol h^{-1} g^{-1} (also outlying) measured for the black phosphorus/Ti_3C_2/g-C_3N_4 composite and g-C_3N_4 were obtained by Song et al. [39]. The calculated medians of the HER rates of @/MXene/g-C_3N_4, MXenes/g-C_3N_4, and g-C_3N_4 were 1620 μmol h^{-1} g^{-1}, 813 μmol h^{-1} g^{-1} and 162 μmol h^{-1} g^{-1}. The Mann–Whitney (M–W), Kolmogorov–Smirnov (K–S) and Mood´s median (MM) confirmed the difference between MXenes/g-C_3N_4 and g-C_3N_4 ($p_{MW}=0.007$, $p_{KS}=0.006$, and p_{MM} 0.005) but the difference between @/MXene/g-C_3N_4 and MXenes/g-C_3N_4 was not confirmed ($p_{MW}=0.270$, $p_{KS}=0.314$, and $p_{MM}=0.147$). All the reviewed articles referred to the significant improvement of the photocatalytic activity of g-C_3N_4 by adding the MXenes which was confirmed by this testing. However, adding some co-catalysts to MXenes/g-C_3N_4 does not lead to a further significant increase of the HER performance. It indicates that the surface (vacancy) and heterojunction engineering of the MXenes/g-C_3N_4 heterojunction is likely more important than the synthesis of the more complex @/MXene/g-C_3N_4 composites.

The HER performance was also compared with other works in which g-C_3N_4 was used for the fabrication of some composites, see Table 2. According to the used statistical tests these results are similar to those obtained by all the @/MXene/g-C_3N_4 and MXene/g-C_3N_4 composites ($p_{MW}=0.654$, $p_{KS}=0.885$, and $p_{MM}=0.740$). In addition, the AQE values obtained with all the composites (@/MXene/g-C_3N_4 and MXene/g-C_3N_4) are also similar to those listed in Table 2 ($p_{MW}=0.184$ and $p_{KS}=0.386$, and $p_{MM}=0.273$).

4 The degradation of the organic compounds

The photocatalytic degradation of the organic compounds is based on the direct reaction of the photoinduced holes with the organic molecules and on the reactions of the radicals formed by the various reaction mechanisms of the electrons and oxygen dissolved in an aqueous phase [61] as follows

$$g\text{-}C_3N_4 + h\upsilon \rightarrow e^-\left(g\text{-}C_3N_4\right) + h^+(g\text{-}C_3N_4) \quad (6)$$

$$e^- + O_2 \rightarrow O_2^{\bullet -} \quad (7)$$

$$O_2^{\bullet -} + H^+ \leftrightarrows HO_2^{\bullet} \quad (8)$$

$$2\,HO_2^{\bullet} \rightarrow H_2O_2 + O_2 \quad (9)$$

$$H_2O_2 + e^- \rightarrow OH^{\bullet} + OH^- \quad (10)$$

Table 2 The HER performance of the other g-C_3N_4 based photocatalysts

Photocatalysts/statistics	Rate (μmol g^{-1} h^{-1})	AQE (%) at 420 nm	Hole scavenger	References
CdS/g-C_3N_4	3670	2.03	Methanol	[46]
CeO_2/g-C_3N_4	203.6	8.94	TEOA	[47]
CoO/g-C_3N_4	262.8	4.93	Ethanol	[48]
$Co_3(PO_4)_2$/g-C_3N_4	375.6	1.32	None	[49]
Fe_2O_3/g-C_3N_4	38.2	2.1	TEOA	[50]
Pt-CdS/ g-C_3N_4-MnO_x	924.4	1.75	None	[51]
N doped g-C_3N_4	3579	27.8	Lactic acid	[52]
$Ni(OH)_2$/g-C_3N_4	21	2.78	TEOA	[53]
$ZnIn_2S_4$/g-C_3N_4	1650	18.2	TEOA	[54]
CoS/ g-C_3N_4/NiS	1930	16.4	TEOA	[55]
1TMoS_2/g-C_3N_4	4426	13.55	TEOA	[56]
NiS/g-C_3N_4	1346	7.67	TEOA	[57]
Ru-CoP/g-C_3N_4	1173	3.49	TEOA	[58]
Co(Mo-Mo_2C)/g-C_3N_4	11.29	6.7	TEOA	[59]
C_3N_5/g-C_3N_4	3330	20.6	TEOA	[60]

$$H_2O_2 + h\upsilon \rightarrow 2OH^{\bullet} \quad (11)$$

The whole degradation reaction of an organic compound can be written as

$$OH^{\bullet} + O_2^{\bullet -} + h^+ + \text{organic compound} \rightarrow CO_2 + H_2O + \text{other products} \quad (12)$$

Most of the reviewed articles evaluated the degradation of the organic compounds as the first-order reaction and in some cases reaction rate constants were published. One of the first articles on this topic reported Ag-decorated g-C_3N_4 and Ti_3C_2 ternary plasmonic photocatalysts for the degradation of aniline [62]. The highest degradation performance of 81.8% was reached after 8 h. The highest rate constant was 0.172 min^{-1}; the rate constant for g-C_3N_4 was 0.039 min^{-1}. The Ag clusters were prepared by photodeposition. The source of irradiation was a 300 W Xenon lamp with a 420 nm cut-off filter.

The composite Ti_3C_2/g-C_3N_4 was investigated for the degradation of ciprofloxacin under a light source with a 400 nm cut-off filter [63]. The ciprofloxacin (CIP) was completely decomposed after 150 min. The rate constant was 0.035 min^{-1} for the composite and 0.016 min^{-1} for pure g-C_3N_4.

The photocatalytic activity of a TiO_2@Ti_3C_2/g-C_3N_4 ternary heterostructure was studied by Ding et al. [64]. The O/OH-terminated Ti_3C_2 and the by-product TiO_2 could act as excellent supporters for migrating electrons. A photocatalysis was performed in terms of the degradation of aniline and Rhodamine B (RhB). After 8 h, 76.4% of the aniline was removed. The majority (98.2%) of RhB was removed after 60 min. For this purpose, a 300 W Xe lamp (100 mW cm^{-2}) was used.

Also, the nanotubes of the TiO_2@Ti_3C_2/g-C_3N_4 composites were prepared by Ti meshes by anodization, the chemical vapor deposition method, and in-situ growth. They were used for the degradation of RhB and tetracycline (TC) with the degradation rates of 0.0370 min^{-1} and 0.0091 min^{-1}, respectively [65]. 96.04% of RhB was removed after 90 min and 85.12% of the tetracycline was removed after 3 h.

He et al. [66] referred to using the composite of the 2D/2D heterostructure of Ti_3C_2/g-C_3N_4 to activate peroxymonosulfate for the removal of diclofenac. The optimal degradation rate of 0.21 min^{-1} was achieved when pure g-C_3N_4 nanosheets provided a rate of 0.071 min^{-1}. Due to the synergistic effect of the photocatalysis and peroxymonosulfate, $^1O_2$ was generated as a primary reactive species. Almost 95% of diclofenac was degraded in 30 min. The photocatalytic experiments were performed under a 300W Xe lamp simulating solar irradiation.

Dong et al. [36] synthetized the 2D/2D Ti_3C_2/g-C_3N_4 composites in a semi-closed system and tested for the degradation of tetracycline hydrochloride. The highest degradation performance reached 84.4% during 120 min while single g-C_3N_4 reached only 29.0%. The largest rate constant was 0.0141 min^{-1} for the composite and 0.0028 min^{-1} for g-C_3N_4.

Wu et al. [37] fabricated the 2D/2D/2D Bi_2WO_6/g-C_3N_4/Ti_3C_2 composites. The well-matched band structure favours the formation of a Z-scheme heterojunction. This composite was used for the photocatalytic degradation of CIP. The rate

constant was 0.058 min^{-1}; 87.7% of the CIP was degraded within 70 min.

$TiO_2/Ti_3C_2/g\text{-}C_3N_4$ heterojunction photocatalysts were also fabricated by Luo et al. [67]. The degradation of methylene orange achieved the maximal value of 93.1%. The highest rate constant was 0.02095 min^{-1} in comparison with 0.00578 min^{-1} of pure $g\text{-}C_3N_4$. The degradation of the best photocatalyst was also confirmed for the degradation of RhB (90.47%) and methylene blue (MB) (91.14%).

$Ti_3C_2/g\text{-}C_3N_4$ composites were prepared by the intercalation of the Ti_3C_2 layers into $g\text{-}C_3N_4$ layers to obtain an efficient heterojunction. The photocatalysts were used for the oxidation of pyridine and thiophene for fuels [68]. Dissolved oxygen (from the atmosphere) formed superoxide radicals and assisted in the oxidation of pyridine to nitrate and thiophene to sulphate. The band gap of Ti_3C_2 was determined at 1.09 eV.

A 2D/2D Ti_3C_2/porous $g\text{-}C_3N_4$ van der Waals heterostructure photocatalyst was synthetized by Liu et al. [69]. A porous $g\text{-}C_3N_4$ was prepared by a hard template method. Packed silica spheres (50 nm) were employed as a templating agent. It was showed that a 98% phenol removal during the day and even a 32% degradation during the night was reached which was explained by the storage of photoinduced electrons and holes under solar irradiation. It was simulated by a 500 W Xenon lamp ($\lambda > 400$ nm).

Cationic dyes MB and RhB were photodegraded in the presence of hybrid chitosan and $Ti_3C_2/g\text{-}C_3N_4$ nanosheets [70]. The presence of the –OH terminal groups of Ti_3C_2 was confirmed. The –OH termination, providing high conductivity and outstanding hydrophilicity, is highly efficacious in the removal of organic molecules. The degradation efficiency was 99.1% for MB in 60 min and 98.5% for RhB in 40 min. The degradation pathways were studied in detail. The photocatalytic experiments were performed under a 250 W Xe-lamp (400–800 nm). The MB and RhB results were verified by the degradation of other dyes, such as Methyl Orange, Malachite Green, and Orange Green.

Embedding few-layer Ti_3C_2 into alkalized $g\text{-}C_3N_4$ nanosheets was reported by Yi et al. [71]. The photocatalytic degradation was tested on tetracycline with an efficiency of 77% during 60 min. The amine groups in $g\text{-}C_3N_4$ were supposed to interact with the carbon layers and the -OH groups of Ti_3C_2, building a van der Waals heterostructure between the two constituents of the composite. Moreover, $AgNO_3$ was added into the reaction mixture. Electrons trapped with the MXene possibly reduced the Ag^+ ions to Ag particles forming another Schottky junction that suppresses the charge recombination process and slightly improved the photocatalytic degradation.

A high-energy ball milling technology was applied for a one-step synthesis of the $TiO_2/Ti_3C_2/g\text{-}C_3N_4$ composites for the visible light degradation of Methyl Orange [72]. This ternary composite exhibited a 90.55% performance after 120 min. Ti_3C_2 acted as a transport medium for this Z-type heterojunction structure. TiO_2 promoted the separation of the photocatalytic carriers and thus the photocatalytic reaction.

Samarium-doped $Ti_3C_2/g\text{-}C_3N_4$ was synthetized by the prepolymerization of $g\text{-}C_3N_4$ and the solid mixture calcination by Yu et al. [73]. The degradation of CIP under visible irradiation achieved > 99% within 60 min. The Sm-doping was supposed to improve the transfer of photoinduced electrons and Ti_3C_2 broadened the light absorption and improved the charge carrier migration efficiency.

The already mentioned work of Liu et al. [43] about the $Ti_3C_2/g\text{-}C_3N_4$ nanosheets for the HER was also tested for the degradation of RhB. The highest degradation rate was 0.194 min^{-1} and with a degradation efficiency of 78.5%.

The $Ti_3C_2/g\text{-}C_3N_4$ nanosheets were tested by Liu et al. [74] for their photocatalytic redox capacity. The degradation of levofloxacin reached 72% using a composite with a 1wt% of Ti_3C_2. A photocatalytic improvement was achieved by the faster separation of the photoinduced electrons and holes, the higher light response ability, and the more active sites. The successful formation of the 2D/2D Schottky junction and the Ti–N bonds between $g\text{-}C_3N_4$ and Ti_3C_2 were observed.

Atrazine was phototactically degraded by using a π–π stacked pyromellitic dimide (PDI) $TiO_2/Ti_3C_2/g\text{-}C_3N_4$ photocatalyst [75]. The degradation was activated by peroxymonosulphate. The π–π interaction in $PDI/g\text{-}C_3N_4$ induced the delocalization of the photoelectrons and thus promoted their migration. The highest degradation efficiency reached 75%. The degradation was performed under visible irradiation (the Xe lamp) with a 420 nm cut-off filter.

The tetracycline, ciprofloxacin, bisphenol A (BPA), and RhB degradation under visible light irradiation was performed in the presence of graphene layers anchored on $TiO_2/g\text{-}C_3N_4$ which was synthetized from Ti_3C_2 by a one-step in-situ calcination [76]. The obtained degradation rates were 0.02442 min^{-1} for TC, 0.01675 min^{-1} for CIP, 0.01935 min^{-1} for BPA, and 0.05586 min^{-1} for RhB. The best removal efficiencies were 83.5% (TC in 80 min), 61.7% (CIP in 60 min), 79.5% (BPA in 70 min), and 98.0% (RhB in 50 min).

Tetracycline together with dyes, such as Congo red (CR) and Trypan blue (TB), were removed by composite membranes made of $Ti_3C_2/g\text{-}C_3N_4$ and polyethersulphone [77]. The presence of –F and –O terminations was confirmed. The membranes were irradiated by a 70 W golden lamp for 8 h. The achieved removal efficiency was 98% for CR, 96% for TB, and 86% for TC.

The fabrication of the carbonized cellulose nanofibrils/$Ti_3C_2/g\text{-}C_3N_4$ was reported by Zu et al. [78]. This

heterojunction composite was then applied for the photocatalytic degradation of MB, RhB, and TC with an efficiency 96.5%, 95.4%, and 86.5% respectively. The irradiation source was a 300 W Xe arc lamp with a 420 nm filter. The photocatalytic experiments took 210 min.

The Ti_3C_2/g-C_3N_4 Schottky junction photocatalyst was prepared to be used for the degradation of arbidol hydrochloride (ABLH) as a drug against COVID-19. Ti_3C_2 was terminated by the –F and –O species. The composite containing 0.5% of Ti_3C_2 was able to remove 99.2% of the ABLH during 150 min under visible irradiation (the 300 W Xe lamp). The highest rate constant of the composite was 0.02959 min^{-1} while that of g-C_3N_4 was 0.01111 min^{-1}.

Graphitic carbon nitride coupled with the Ti_3C_2 derived amorphous Ti-peroxo heterojunction for the photocatalytic degradation of rhodamine B and tetracycline was prepared by Tu et al. [79]. The RhB highest rate constant of the composite containing 35% of g-C_3N_4 was measured at 0.051 min^{-1} and that for bare g-C_3N_4 was 0.0029 min^{-1} using a 270 W Xe lamp ($\lambda > 420$ nm). In the case of TC, the best performing composite containing 25% of g-C_3N_4 demonstrated a rate constant of 0.0208 min^{-1}. A constant of 0.0003 min^{-1} was found for g-C_3N_4.

Zhou et al. [80] synthetized the 2D/2D Mo_2C/g-C_3N_4 Van der Waals heterojunction composites. Their photocatalytic performance was tested by the degradation of TC. The highest rate constant of 0.066 min^{-1} was obtained for the composite with 2% of Mo_2C while the constant of bare g-C_3N_4 was 0.017 min^{-1}. The Mo_2C enhanced the light absorption capacity and served as an electron trap to elongate the lifetime of the charge carriers.

Methylene blue was also degraded by g-C_3N_4 on which the Ti_3C_2 particles were loaded as reported by Nasri et al. [81]. A 1 wt% MXene/g-C_3N_4 heterostructure photocatalyst achieved the 60% degradation of methylene blue during 180 min. A 500 W halogen lamp was used as the irradiation source. The band gap of this most active photocatalyst was 2.53 eV.

BiOBr/Ti_3C_2/g-C_3N_4 Z-scheme heterostructure photocatalysts were tested for the TC degradation [82]. The Xe lamp with 400–800 nm cut-off filters was applied for this purpose. TC was completely removed after 30 min and the best rate constant was 0.204 min^{-1}. The optimal BiOBr and g-C_3N_4 composite was investigated. The proposed mechanism of the charge transfer is demonstrated in Fig. 4.

A novel $MnFe_2O_4$/Ti_3C_2/g-C_3N_4 composite was fabricated by Hou et al. [83] and used for the peroxymonosulphate-assisted photocatalytic degradation of naphthalene. Almost 100% was removed during 45 min. The highest rate constant of 0.09984 min^{-1} was achieved. There existed both free radical and non-radical pathways for the naphthalene degradation, in which singlet oxygen was identified as the main reactive oxygen species as a result of the Mn–Fe

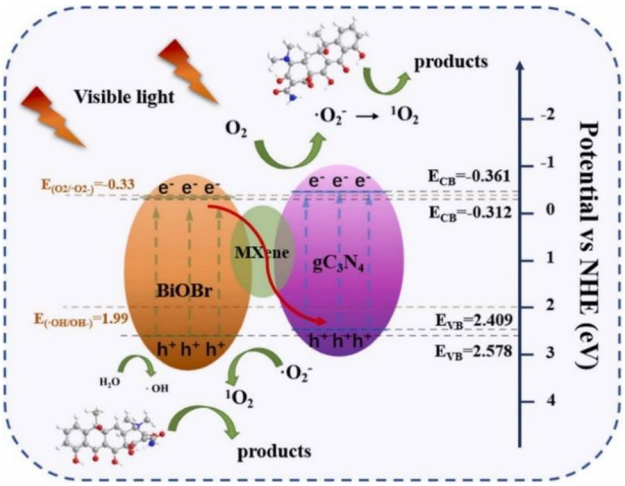

Fig. 4 The proposed mechanism of the charge transfer and separation on the surface of BiOBr/Ti_3C_2/g-C_3N_4 for TC degradation under visible light illumination. Reproduced from Ref. [82]. Copyright (2023), with permission from Elsevier

valence transformation process. The degradation pathway of naphthalene was studied.

4.1 The performance of the organic compound degradation

The degradation efficiency of the organic compounds strongly depends on their types (their chemical structures) and on experimental conditions. The articles included in this work refer to the degradation of various dyes, pharmaceutical products, aniline, naphthalene etc. In general, the decomposition reactions are mostly described by the first-order equation as

$$\frac{c}{c_0} = e^{-kt} \tag{13}$$

where t is time, k is the rate constant, c and c_0 are concentrations at t = t and t = 0, respectively.

A half-life time, which is the time taken for a given concentration to decrease to half of its value, was used as a measure of how the degradation performance of @/MXene/g-C_3N_4, MXenes/g-C_3N_4, and g-C_3N_4 improved. For the half-life time, it is valid that

$$t_{1/2} = \frac{ln2}{k} \tag{14}$$

The half-life time of the first-order reaction remains constant throughout the reaction and is independent of the concentrations. In order to compare the photocatalytic degradation of the various organic compounds at various concentrations, the ratios (r) of the half-times for the individual

organic compounds decomposed in the presence of the MXene based photocatalysts (2) and g-C_3N_4 (1) were calculated as follows

$$r = \frac{t_{1/2}(1)}{t_{1/2}(2)} = \frac{k(2)}{k(1)} \quad (15)$$

The kinetic constants were taken from the reviewed articles if they were published. The ratio is supposed to be dependent on the catalysts used, not on the experimental conditions. The ratios were statistically processed by the already used statistics.

The box and whisker plots are shown in Fig. 5. The basic statistical characteristics were calculated, see Table S3. The outlying ratio of 69.3 (Fig. 5) corresponds to the degradation of tetracycline using the composite of g-C_3N_4 and Ti_3C_2 with the Ti-peroxo heterojunction [79]. The medians were 3.369 and 2.425 for @/MXene/g-C_3N_4 and MXenes/g-C_3N_4 respectively.

These median values (higher that 2 and 3) tell us that the photocatalytic activity of g-C_3N_4 was highly improved by adding the MXenes. On the contrary, it was found that some co-catalysts added to MXene/g-C_3N_4 do not improve its photocatalytic degradation ($p_{MW} = 0.751$, $p_{KS} = 0.869$, and $p_{MM} = 0.414$) which means the surface and heterojunction engineering are more important.

A comparison with other photocatalysts based on g-C_3N_4 was not performed because the degradation efficiency depends on the individual organic compounds as already mentioned. Their redox potentials have different positions toward the valence and the conduction bands of g-C_3N_4 which means that the photoinduced holes are not always involved in the photocatalytic reactions, see Eq. (12). In addition, the organic compounds differ in their adsorption properties to the photocatalysts.

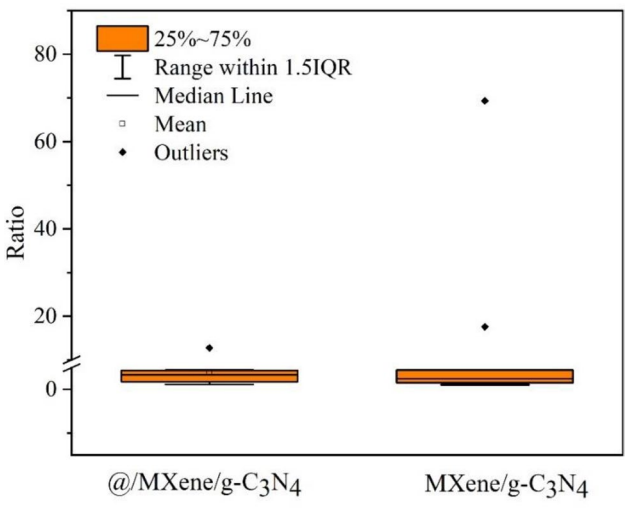

Fig. 5 Box plots of ratios of the half-life times of organic compounds photocatalytically degraded using @/MXene/g-C_3N_4 and MXene/g-C_3N_4 composites

5 The reduction of carbon dioxide

MXenes have been also used as co-catalysts for the photocatalytic reduction of carbon dioxide. Some redox reactions (versus NHE at pH = 7) are summarized below [84]:

$$CO_2 + 2\,H^+ + 2\,e^- \rightarrow HCOOH \quad E^o = -0.61\ V \quad (16)$$

$$CO_2 + 2\,H^+ + 2\,e^- \rightarrow CO + H_2O \quad E^o = -0.53\ V \quad (17)$$

$$CO_2 + 4\,H^+ + 4\,e^- \rightarrow HCHO + H_2O \quad E^o = -0.48\ V \quad (18)$$

$$CO_2 + 6\,H^+ + 6\,e^- \rightarrow CH_3OH + H_2O \quad E^o = -0.38\ V \quad (19)$$

$$CO_2 + 8\,H^+ + 8\,e^- \rightarrow CH_4 + 2\,H_2O \quad E^o = -0.24\ V \quad (20)$$

$$2\,H^+ + 2\,e^- \rightarrow H_2 \quad E^o = -0.41\ V \quad (21)$$

The TiO_2/Ti_3C_2/g-C_3N_4 S-scheme photocatalysts were constructed by He et al. [85]. Ti_3C_2 MXene quantum dots were deposited on the 2D/2D van der Waals heterojunction of TiO_2 and g-C_3N_4. 2D mesoporous TiO_2 nanosheets were synthesized by a hydrothermal induced solvent-confined monomicelle self-assembly. Reduction products, such as CO and CH_4, reached their maxima at 4.39 and 1.20 μmol g^{-1} h^{-1}. The S-scheme heterojunction at the TiO_2/g-C_3N_4 interface and the Schottky heterojunction at the g-C_3N_4 and the quantum dots interface mostly affected the photocatalytic activity.

Tahir and Tahir [86] constructed a 2D/2D/2D O-C_3N_4/bentonite/Ti_3C_2 heterojunction composite. The bentonite/Ti_3C_2 composite demonstrated high light absorption and fast charge separation and transportation. The CO_2 reduction to CH_4 and CO was performed under a 35 W HID lamp with a maximum intensity at 420 nm (20 mW cm^{-2}). The CO evolution rate was 365 μmol g^{-1} h^{-1} (76 μmol g^{-1} h^{-1} with pure g-C_3N_4) and the CH_4 one was 955 μmol g^{-1} h^{-1} (33 μmol g^{-1} h^{-1} with g-C_3N_4). The AQE values were measured at 1.203% for CO and 3.146% for CH_4 (Fig. 6).

The photocatalytic reduction of carbon dioxide to carbon monoxide and methane was investigated by Tang et al. [87] using g-C_3N_4 decorated with alkalinized Ti_3C_2. The highest production rates were 11.21 μmol g^{-1} h^{-1} for CO and 0.269 μmol g^{-1} h^{-1} for CH_4. The AQE values were estimated at 0.0099% for both CO and CH_4 (at 420 nm). The optimal content of Ti_3C_2 was 5 wt%. The adsorption of CO_2

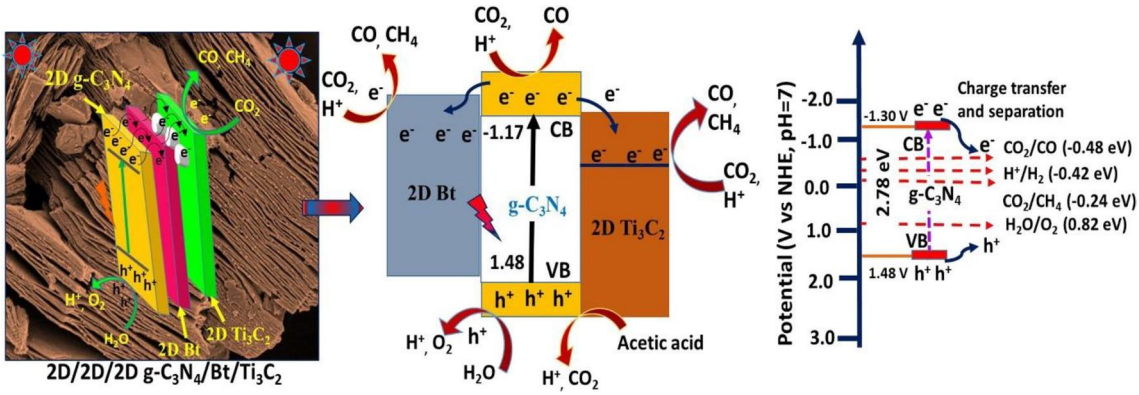

Fig. 6 Proposed mechanism for the photocatalytic CO_2 conversion to CO and CH_4 over the g-C_3N_4/bentonite/Ti_3C_2 heterojunction system under visible light. Reproduced from Ref. [86]. Copyright (2020), with permission from Elsevier

was attributed to the Ti_3C_2 surface modified with the -OH groups.

The Ti_3C_2/g-C_3N_4 heterojunction with a double role of urea was synthetized by Yang et al. [88]. The urea was used for the synthesis of g-C_3N_4 and also for the exfoliation of Ti_3C_2. The optimal sample (10 wt% of Ti_3C_2) possessed the best photocatalytic performance with the rates of 5.19 μmol h^{-1} g^{-1} for CO and 0.044 μmol h^{-1} g^{-1} for CH_4. The -F terminal groups were fully substituted with -OH and -O ones which was beneficial for Ti_3C_2 to trap the photoinduced electrons.

Similar Ti_3C_2/g-C_3N_4 photocatalysts were fabricated by Hu et al. [89]. The Ti_3C_2 was anchored on g-C_3N_4 via NH_x-Ti bonds. The optimized materials containing 2 wt% of Ti_3C_2 exhibited a CH_4 production rate of 0.99 μmol h^{-1} g^{-1} under visible irradiation (λ > 420 nm). This high performance was mainly attributed to the synergistic effects of the close interfacial interaction, the Schottky junction, and the remarkable conductivity of Ti_3C_2.

The ultrathin S-scheme heterojunction photocatalyst, based on few-layer g-C_3N_4 and monolayer Ti_3C_2, was constructed by Yang et al. [90]. An ultrathin heterojunction g-C_3N_4/TiO_2/C was synthetized through electrostatic self-assembly and calcination. CO and CH_4 were the main products of the CO_2 reduction. The highest achieved reduction rates using this kind of photocatalyst were 25.96 μmol h^{-1} g^{-1} for CO and 3.70 μmol h^{-1} g^{-1} for CH_4. The CO_2 reduction was performed in an airtight reactor with a certain amount of water under Xe arc lamp irradiation.

The already mentioned authors, Liu et al. [74], also tested their Ti_3C_2/g-C_3N_4 composite for the reduction of CO_2. The highest rate for the CO evolution was 10.67 μmol h^{-1} g^{-1} and that for the CH_4 evolution was 2.64 μmol h^{-1} g^{-1}. The 2D/2D Schottky junction and a new Ti-N bond between g-C_3N_4 and Ti_3C_2 were formed.

Boron-doped g-C_3N_4 was combined with few-layer Ti_3C_2 by electrostatic self-assembly and used for the CO_2 reduction under visible irradiation (a 300 W Xe lamp with λ > 420 nm, 175 mW cm^{-2}) [91]. The observed products were carbon monoxide, methane, and hydrogen. The highest CO_2 reduction yields were 14.4 and 0.80 μmol h^{-1} g^{-1} for CO and CH_4, respectively. The AQE for CO and CH_4 was measured to be 0.0117% at 420 nm.

A 2D/2D $Ti_3C_2T_{A/R}$ MXene coupled g-C_3N_4 heterojunction with the in-situ growth of anatase/rutile TiO_2 nucleates was developed by Khan and Tahir [92]. Etching by high concentrated HF enabled the better conversion of Ti_3C_2 to TiO_2. The composite provided the hydrogen and CO rates of 51.24 and 87.34 μmol h^{-1} g^{-1}, respectively. The photoreactor was equipped with a 35 W Xe lamp with the wavelength of 420 nm (20 mW cm^{-2}). The highest AQE values were 0.732% for CO and 0.430% for H_2.

Mesoporous Ti_3C_2/g-C_3N_4 photocatalysts were fabricated by Li et al. [93] for the CO_2 reduction. Mesoporous structures possess abundant absorption sites for the CO_2 molecules and reduces the recombination of the electrons and holes. The methane production rate was 2.117 μmol h^{-1} g^{-1}, which was 2.4 times more than the bare mesoporous g-C_3N_4. The CO rate was 3.98 μmol h^{-1} g^{-1} (all with a 300 W Xe lamp).

A 2D Ti_3C_2 decorated Z-scheme $BiOIO_3$/g-C_3N_4 heterojunction was fabricated by Hong et al. [94] and used for the CO_2 reduction. The optimal photocatalytic efficiency of 5.88 and 1.55 μmol h^{-1} g^{-1} was reached for CO and CH_4, respectively, under the visible irradiation of the 300 W Xe lamp with a cut-off filter for 420 nm.

The composite consisting of 2D V_2C nanosheets coupled 2D with porous g-C_3N_4 was designed by Madi et al. [95]. The highest performance of 37.75 and 51.25 μmol h^{-1} g^{-1} of CO and CH_4, respectively, was reached with the composite containing 15% of V_2C. These values are 6.7 and 1.3 times

higher than using bare g-C_3N_4. An irradiation source was a 35 W HID Xe lamp. (20 mW cm^{-2}).

Carbon vacancy-mediated exciton dissociation in the Ti_3C_2/g-C_3N_4 Schottky heterojunction photocatalysts was synthetized by Song et al. [96]. The synergy between the vacancy engineering and the Schottky junction was studied. The optimal photocatalyst contained 20% of Ti_3C_2. Graphitic carbon nitride with C vacancies was prepared for this purpose. The highest CO yield was 20.54 µmol h^{-1} g^{-1} which was 7.3 times higher than that of bare g-C_3N_4. The 300 W Xe arc lamp was equipped with a 400 nm cut-off filter.

A novel hybrid g-C_3N_4/ZnO/Ti_3C_2 was recently synthetized by Li et al. [97]. In the interface of g-C_3N_4/ZnO, g-C_3N_4/Ti_3C_2 and ZnO/Ti_3C_2, an internal electric field was generated. The electron transfer directions were from g-C_3N_4 to ZnO, from ZnO to Ti_3C_2 and from g-C_3N_4 to Ti_3C_2. Due to the metallic properties of Ti_3C_2 (electrons migrate to Ti_3C_2 more easily), the CO production rate was increased up to 6.41 µmol h^{-1} g^{-1} and the CH_4 rate up to 0.27 µmol h^{-1} g^{-1}. The AQEs were measured at 0.22% for CO and 0.06% for CH_4 at 350 nm.

5.1 The performance of the CO_2 reduction

All the above-mentioned information is summarized in Table S4. The CO results were analysed by the box and whisker plots and the highest (outlying) values were the CO rates of 365 µmol h^{-1} g^{-1} for O-C_3N_4/bentonite/Ti_3C_2 and 76 µmol h^{-1} g^{-1} for g-C_3N_4 [86], see Fig. 7.

The calculated medians of the CO rates of @/Ti_3C_2/g-C_3N_4, Ti_3C_2/g-C_3N_4, g-C_3N_4 were 5.88 µmol h^{-1} g^{-1}, 9.93 µmol h^{-1} g^{-1} and 1.69 µmol h^{-1} g^{-1}. For other statistics see Table S5. A significant improvement of photocatalytic activity by adding MXenes to g-C_3N_4 is obvious

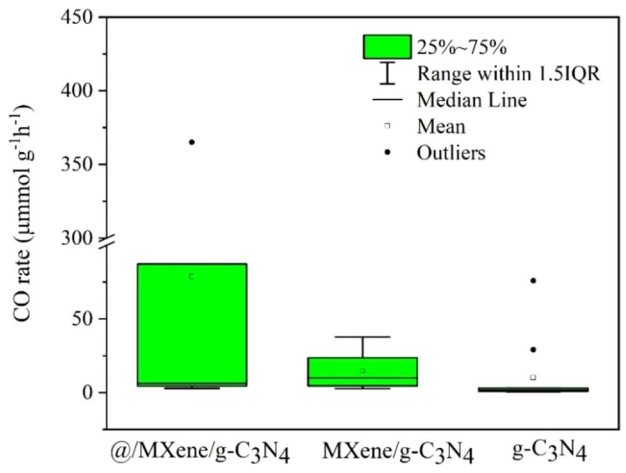

Fig. 7 Box plots of the CO rate of @/$MXene_2$/g-C_3N_4 (left), MXene/g-C_3N_4 (centre), and g-C_3N_4 (right)

(p_{MW} = 0.023 and p_{KS} = 0.009, and p_{MM} = 0.006). Comparing the @/MXene/g-C_3N_4 and MXene/g-C_3N_4 data by the statistical tests (p_{MW} = 0.948, p_{KS} = 0.784, and p_{MM} = 0.280) shows that no difference between these two datasets was found which means that the added co-cocatalysts did not play an important role in the photocatalytic performance.

The same analysis was performed for the CH_4 production rate. The highest (outlying) value of 955 µmol h^{-1} g^{-1} obtained using the O-C_3N_4/bentonite/Ti_3C_2 complex was detected [86]. The calculated medians of the CH_4 rates measured in the presence of the @/MXene/g-C_3N_4, MXene/g-C_3N_4, g-C_3N_4 composites were 1.20 µmol h^{-1} g^{-1}, 0.990 µmol h^{-1} g^{-1} and 0.200 µmol h^{-1} g^{-1}. Other statistic parameters are shown in Table S6. The already used tests (p_{MW} = 0.871, p_{KS} = 0.997, and p_{MM} = 0.558) indicated that the CH_4 rates corresponding to the @/MXene/g-C_3N_4 and MXene/g-C_3N_4 composites were not found to be statistically different. Similarly, as in the CO production, the added co-catalysts did not influence the CH_4 production.

However, the adding of MXene to g-C_3N_4 did not show the important photocatalytic effect (p_{MW} = 0.174 and p_{KS} = 0.294, and p_{MM} = 0.147). Based on the used nonparametric statistical testing results, the reduction of CO_2 to CH_4 was not found to be significantly affected by the heterojunction of g-C_3N_4 with MXenes.

The CO_2 reduction performance was compared with other works using some g-C_3N_4 based composites. The data in Table 3 indicate that concerning all the @/MXene/g-C_3N_4 and MXene/g-C_3N_4 composites the CO rates are comparable with the others based on g-C_3N_4 (p_{MW} = 0.234, p_{KS} = 0.289, and p_{MM} = 0.180). In the case of CH_4, the statistical testing confirmed that the MXene and g-C_3N_4 composites provided different (lower) performance than the other g-C_3N_4 based composites (p_{MW} = 0.011 and p_{KS} = 0.003, p_{MM} = 0.001), see Figure S1. The AQE values were not compared with those in Table 3 because only four articles reported these data.

The findings concerning the CO_2 reduction to CH_4 can be explained by the low adsorption of CO on the MXenes. Since the reduction of CO_2 takes place in a step-wise process [113], after its reduction to CO this oxide is mostly released [114] and its further reduction to CH_4 is limited. It also explains the lower rates of CH_4 in comparison with the rates of CO, see Figs. 7 and 8.

6 The redox reactions of nitrogen

6.1 Nitrogen reduction reaction

The nitrogen reduction reaction (NRR) to ammonia performed by MXene-derived TiO_2@C/g-C_3N_4 was reported by Liu et al. [115]. This composite was prepared via a facile one step calcination of a mixture of Ti_3C_2 and melamine.

Table 3 CO_2 reduction performance of some g-C_3N_4 based photocatalysts

Photocatalysts/statistics	Rate CO (μmol g^{-1} h^{-1})	Rate CH_4 (μmol g^{-1} h^{-1})	AQE (%) at 420 nm	References
NiS_2/g-C_3N_4	10.68		2.03	[98]
SnO_2/B-P-g-C_3N_4		30.6	2.02	[99]
Phosphorylated/g-C_3N_4	7.7	14.6	0.86	[100]
Eu(III)/g-C_3N_4		3.8	1.6	[101]
Ag/g-C_3N_4	179.6		0.25	[102]
WO_3/g-C_3N_4	48.7		2.21	[103]
Au/TiO_2/g-C_3N_4	21.7	37.4	1.91	[104]
NiAl-LDH/rGO/g-C_3N_4	2.6	20	0.99	[105]
TiO_2/C/Pt/g-C_3N_4	14.7	65.6	5.67	[106]
FeV_2O_4/g-C_3N_4	5.79		5.79	[107]
$BiO_{(1-x)}Br$/g-C_3N_4	13.11		0.098	[108]
Nb_2O_5/g-C_3N_4	253.34	68.11	4.95	[109]
Bi_3O_4Cl/g-C_3N_4	6.6	1.9	0.68	[110]
Bi_2O_3/Bi_2WO_6/g-C_3N_4	29.3		1.3	[111]
Bi_2S_3/g-C_3N_4	54.74	12.52	2.31	[112]

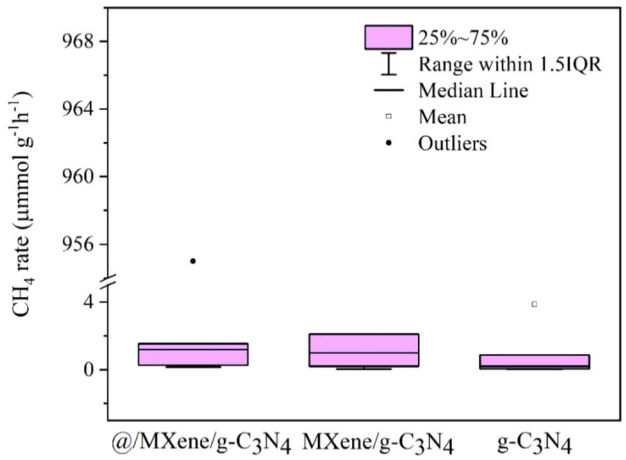

Fig. 8 Box plots of the CH_4 rate of @/MXene/g-C_3N_4 (left), MXene/g-C_3N_4 (centre), and g-C_3N_4 (right)

The formation of C–Ti–O bonds was confirmed. The NH_3 production rate of 250.6 μmol h^{-1} g^{-1} was achieved under visible irradiation (the 300 W Xe lamp, λ > 420 nm). Methanol was used as the scavenging reagent. The AQE was 0.14% at 420 nm.

Nb_2O_5/C/Nb_2C/g-C_3N_4 heterojunction photocatalysts were constructed by Jiang et al. [116]. The photocatalysts were prepared by growing Nb_2O_5 on Nb_2C and then forming g-C_3N_4 nanosheets in situ on Nb_2O_5/C/Nb_2C. The optimized photocatalyst with a Nb_2O_5/C/Nb_2C g-C_3N_4 ratio of 1:1 exhibited the NRR rate of 365 μmol h^{-1} g^{-1}. With the optimized pH 9 adjusted by a NaOH solution, the NRR rate increased to 927 μmol h^{-1} g^{-1}. Methanol was used as the scavenger as well.

The already mentioned work of Liu et al. [74] about the Ti_3C_2/g-C_3N_4 nanosheets also reported the production of NH_3 with the rate of 601 μmol L^{-1} h^{-1} g^{-1}, which is 3.64 times higher than that of g-C_3N_4 (203 μmol L^{-1} h^{-1} g^{-1}).

Sun et al. [117] synthetized a 2D/2D Ti_3C_2/N-defect g-C_3N_4 heterostructure composite for the NRR. The heterostructure was constructed by filling the -O terminating groups of Ti_3C_2 in the N-defects of g-C_3N_4 forming C-O-Ti interactions. The defects were prepared by the acid-assist thermal polymerization reaction of melamine and citric acid. The highest reported reaction rate was 341 μmol h^{-1} g^{-1}.

The Schottky junction photocatalysts were synthetized from hollow g-C_3N_4 decorated with the partly reduced quantum dots of Ti_3C_2 [118]. The surface of Ti_3C_2 was rich in Ti^{3+} sites and oxygen vacancies which facilitated the capture and activation of the nitrogen molecules for the subsequent ammonia formation. The highest NH_3 production rate was 328.9 μmol h^{-1} g^{-1} under white light (300 mW cm^{-2}, λ = 300–780 nm). Pristine g-C_3N_4 had the rate of 124.2 μmol h^{-1} g^{-1}.

6.2 NO oxidation reaction

Ti_3C_2 modified g-C_3N_4 was used for the photocatalytic NO removal [119]. The formation of a build-in electron field could lead to the photo-induced electrons accumulation on Ti_3C_2 to promote the activation of O_2, which promoted the generation of radical species and the subsequent photocatalytic surface reaction of NO. The photocatalytic oxidation was performed under visible irradiation (λ > 420 nm) and NO was oxidized by oxygen derived radicals to nitrite and nitrate.

The heterojunction photocatalyst Ti_3C_2@TiO_2/g-C_3N_4 was constructed by Zhang et al. [120] and applied for the nitric oxide removal as well. The two-dimensional Ti_3C_2 was partially oxidized to form TiO_2-Ti_3C_2 nanosheets by controlled oxidation conditions. A removal efficiency of 28.9% was reached. A small amount of NO_2 (18.75 ppb), as a reaction product, was determined. The other reaction species were nitrate and nitrite.

The oxidation removal of NO using Ti_3C_2-derived TiO_2@C coupled with g-C_3N_4 was also published by Wang et al. [121]. The Z-scheme heterojunction enabled the enhanced photocatalytic NO removal. These authors reached a 94% removal efficiency of the nitric oxide using atomized H_2O_2 under a 500 W Xenon lamp (a 420 nm cut-off filter), see Fig. 9.

Ternary g-C_3N_4/TiO_2/Ti_3C_2 MXene S-scheme heterojunction photocatalysts were fabricated by Hu et al. [122] and tested for the oxidation of NO. TiO_2/Ti_3C_2 was prepared by the partial oxidation of Ti_3C_2. G-C_3N_4 polymerized from melamine on the surface of TiO_2/Ti_3C_2.The removal efficiency was 66.3% after 30 min. The other reactions products were NO_2 and nitrate.

The similar reaction with H_2O_2 but using a 2D/0D/2D g-C_3N_4/TiO_2@C aerogel was published by the same group of authors [123]. The removal efficiency of 90.7% was achieved during 50 min. The main reaction product was nitrate.

There are not enough data in the literature concerning the MXene and g-C_3N_4 composites for both the nitrogen reduction reaction and the NO oxidation reaction yet. Therefore, the statistical testing was not performed for these photocatalytic reactions.

7 Miscellaneous

A Ti_3C_2/porous g-C_3N_4 interfacial Schottky junction photocatalyst was employed for the production of hydrogen peroxide by Yang et al. [124]. The highest H_2O_2 production rate of 2.20 μmol L^{-1} min^{-1} under visible light irradiation ($\lambda > 420$ nm) was 2.1 times higher than that in the presence of pristine porous g-C_3N_4. The interfacial Schottky junction was fabricated by an electrostatic self-assembly process.

Ti_3C_2 quantum dot-modified defective inverse opal g-C_3N_4 via a facile electrostatic self-assembly method was prepared by Lin et al. [125]. The opal g-C_3N_4 contained carbon vacancies. The Schottky junction in the interface realized the spatial separation of the electrons and holes. The highest H_2O_2 yield reached 560.7 μmol L^{-1} h^{-1}, which is 9.3 times higher than that of g-C_3N_4 under visible light irradiation.

A work of Wang et al. [126] was devoted to the already described Ti_3C_2/porous g-C_3N_4 composite for the oxidation of 5-hydroxymethylfurfural to 2,5-formylfuran. The composite containing 6% Ti_3C_2 provided a yield higher than

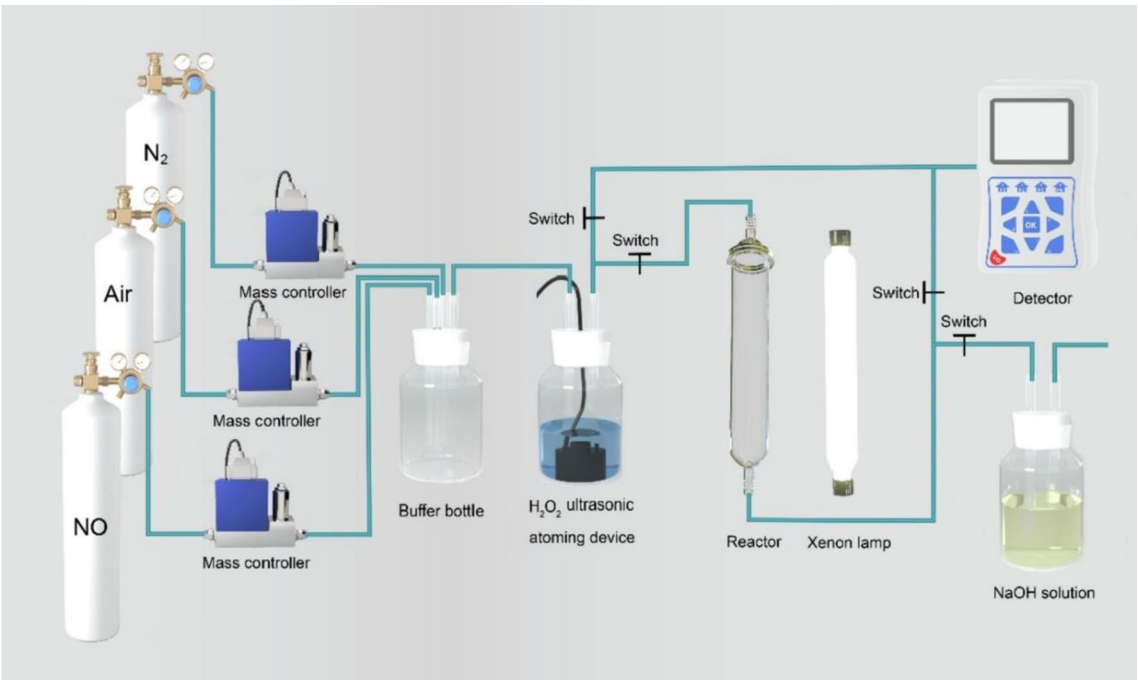

Fig. 9 Schematic diagram of the experimental apparatus for the photocatalytic oxidation method of NO. Reproduced from Ref. [121]. Copyright (2022), with permission from Elsevier

90% during 10 h under visible irradiation. The selectivity was 97%.

Zr_2CO_2/g-C_3N_4 heterostructure photocatalysts were designed, modelled, and tested for the volatile organic compound degradation [127]. The first principal calculations were confirmed by the degradation of formaldehyde, acetone, benzene, and trichloro ethylene. A spectroscopic analysis indicated the Z-scheme formation providing the photocatalytic activity as well as a direct band gap. The theoretical calculations were also performed for other MXenes, such as Ti_2CO_2, Hf_2CO_2, and Sc_2CO_2.

The Ti_3C_2/g-C_3N_4 was also tested for the reduction of U(VI) by Li et al. [128]. U(VI) was reduced to U(IV) forming UO_{2+x}, where $x < 0.25$. The main reducing species was the superoxide radical. The optimal photocatalytic reduction rate for U(VI) was 0.267 min^{-1} under a 500 W Xe lamp. The optimal photocatalyst was able to remove all U(VI) during 15 min.

The authors Makola et al. [129] designed and fabricated a 2D-2D Nb_2CT_x@g-C_3N_4 MXene-based Schottky-heterojunction. They experimentally verified that this material is suitable for photocatalytic applications, however, no photocatalytic tests were performed.

8 Conclusion

The research articles (77 in total) about the photocatalytic application of the MXene and g-C_3N_4 composites were reviewed in this work. The MXene and g-C_3N_4 composites were mostly tested for the photocatalytic degradation of organic compounds (31%), the hydrogen evolution (30%), and the reduction of carbon dioxide (18%). The remaining 21% of chemical reactions were devoted to the redox reactions of nitrogen (13%) and other applications (8%). The CO_2 reduction results were only carbon monoxide and methane.

The majority of articles were devoted to Ti_3C_2 based composites with g-C_3N_4. Only a few articles described the results obtained with the Ni_3C, Nb_2C, Zr_2CO_2, Mo_2C, and V_2C MXenes. The basic mechanism of the MXene/g-C_3N_4 composites´ photocatalytic activity is in the combination of the ability of g-C_3N_4 to absorb visible light and the excellent electron transport properties of Ti_3C_2. The heterojunction formed between both compounds enables the effective separation of electrons and holes photoinduced in g-C_3N_4. Both charge carries can then take part in various photocatalytic reactions without their recombination.

A critical review of the cited articles was performed based on the statistical processing of the reported results. Besides the photocatalytic reduction of CO_2 to CH_4, it was found that MXenes significantly improve the photocatalytic activity of bare graphitic carbon nitride. In addition, it was found that adding some co-catalysts to these MXene/g-C_3N_4 composites do not lead to a further increase in photocatalytic activity. The surface (vacancy) and heterojunction engineering of the MXenes and g-C_3N_4 is likely more important.

The MXene and g-C_3N_4 composites were also compared with the other photocatalysts based on g-C_3N_4, especially in terms of the hydrogen evolution and the reduction of CO_2 to CO. Ongoing research should aim to optimize the properties and performance of these materials and explore their potential in photocatalytic applications, such as the higher HER performance and the reduction of CO_2 to other more useful products. The degradation of organic compounds is also a challenge especially in terms of the application and recycling of the photocatalysts in real conditions. The described materials were obtained and tested in laboratories, but still there is a long way to their practical applications.

Supplementary Information The online version contains supplementary material available at https://doi.org/10.1007/s42823-023-00634-9.

Acknowledgements This work was supported by VSB-Technical University of Ostrava (Project No. SP 2023/034).

Funding Open access publishing supported by the National Technical Library in Prague.

Data availability There are no available data.

Declarations

Conflict of interest The author declares no conflict of interest.

References

1. Wang X, Maeda K, Thomas A, Takanabe K, Xin G, Carlsson JM, Domen K, Antonietti M (2009) A metal-free polymeric photocatalyst for hydrogen production from water under visible light. Nat Mater 8(1):76–80. https://doi.org/10.1038/nmat2317
2. Miller TS, Jorge AB, Suter TM, Sella A, Corà F, McMillan PF (2017) Carbon nitrides: synthesis and characterization of a new class of functional materials. Phys Chem Chem Phys 19(24):15613–15638. https://doi.org/10.1039/C7CP02711G
3. Ong W-J, Tan L-L, Ng YH, Yong S-T, Chai S-P (2016) Graphitic carbon nitride (g-C_3N_4)-based photocatalysts for artificial photosynthesis and environmental remediation: are we a step closer to

achieving sustainability? Chem Rev 116(12):7159–7329. https://doi.org/10.1021/acs.chemrev.6b00075
4. Kessler FK, Zheng Y, Schwarz D, Merschjann C, Schnick W, Wang X, Bojdys MJ (2017) Functional carbon nitride materials—design strategies for electrochemical devices. Nat Rev Mater 2(6):17030. https://doi.org/10.1038/natrevmats.2017.30
5. Kong L, Wang J, Ma F, Sun M, Quan J (2019) Graphitic carbon nitride nanostructures: catalysis. Appl Mater Today 16:388–424. https://doi.org/10.1016/j.apmt.2019.06.003
6. Inagaki M, Tsumura T, Kinumoto T, Toyoda M (2019) Graphitic carbon nitrides (g-C_3N_4) with comparative discussion to carbon materials. Carbon 141:580–607. https://doi.org/10.1016/j.carbon.2018.09.082
7. Li Y, Li X, Zhang H, Fan J, Xiang Q (2020) Design and application of active sites in g-C_3N_4-based photocatalysts. J Mater Sci Technol 56:69–88. https://doi.org/10.1016/j.jmst.2020.03.033
8. Barrio J, Volokh M, Shalom M (2020) Polymeric carbon nitrides and related metal-free materials for energy and environmental applications. J Mater Chem A 8(22):11075–11116. https://doi.org/10.1039/D0TA01973A
9. Zhu B, Zhang L, Cheng B, Yu J (2018) First-principle calculation study of tri-s-triazine-based g-C_3N_4: a review. Appl Catal B 224:983–999. https://doi.org/10.1016/j.apcatb.2017.11.025
10. Wang Y, Mao J, Meng X, Yu L, Deng D, Bao X (2019) Catalysis with two-dimensional materials confining single atoms: concept, design, and applications. Chem Rev 119(3):1806–1854. https://doi.org/10.1021/acs.chemrev.8b00501
11. Naguib M, Kurtoglu M, Presser V, Lu J, Niu J, Heon M, Hultman L, Gogotsi Y, Barsoum MW (2011) Two-dimensional nanocrystals produced by exfoliation of Ti_3AlC_2. Adv Mater 23(37):4248–4253. https://doi.org/10.1002/adma.201102306
12. Biswal L, Nayak S, Parida K (2021) Recent progress on strategies for the preparation of 2D/2D MXene/g-C_3N_4 nanocomposites for photocatalytic energy and environmental applications. Catal Sci Technol 11(4):1222–1248. https://doi.org/10.1039/D0CY02156C
13. Mozafari M, Soroush M (2021) Surface functionalization of MXenes. Mater Adv 2(22):7277–7307. https://doi.org/10.1039/D1MA00625H
14. Kang Z, Khan MA, Gong Y, Javed R, Xu Y, Ye D, Zhao H, Zhang J (2021) Recent progress of MXenes and MXene-based nanomaterials for the electrocatalytic hydrogen evolution reaction. J Mater Chem A 9(10):6089–6108. https://doi.org/10.1039/D0TA11735H
15. Jasim SA, Hadi JM, Opulencia MJC, Karim YS, Mahdi AB, Kadhim MM, Bokov DO, Jalil AT, Mustafa YF, Falih KT (2022) MXene/metal and polymer nanocomposites: preparation, properties, and applications. J Alloys Compd 917:165404. https://doi.org/10.1016/j.jallcom.2022.165404
16. Wang Y, Guo T, Tian Z, Bibi K, Zhang Y-Z, Alshareef HN (2022) MXenes for energy harvesting. Adv Mater 34(21):2108560. https://doi.org/10.1002/adma.202108560
17. Yu S, Tang H, Zhang D, Wang S, Qiu M, Song G, Fu D, Hu B, Wang X (2022) MXenes as emerging nanomaterials in water purification and environmental remediation. Sci Total Environ 811:152280. https://doi.org/10.1016/j.scitotenv.2021.152280
18. Liu X, Chen T, Xue Y, Fan J, Shen S, Hossain MSA, Amin MA, Pan L, Xu X, Yamauchi Y (2022) Nanoarchitectonics of MXene/semiconductor heterojunctions toward artificial photosynthesis via photocatalytic CO_2 reduction. Coord Chem Rev 459:214440. https://doi.org/10.1016/j.ccr.2022.214440
19. VahidMohammadi A, Rosen J, Gogotsi Y (2021) The world of two-dimensional carbides and nitrides (MXenes). Science 372(6547):eabf1581. https://doi.org/10.1126/science.abf1581
20. Shao M, Shao Y, Chai J, Qu Y, Yang M, Wang Z, Yang M, Ip WF, Kwok CT, Shi X, Lu Z, Wang S, Wang X, Pan H (2017) Synergistic effect of 2D Ti_2C and g-C_3N_4 for efficient photocatalytic hydrogen production. J Mater Chem A 5(32):16748–16756. https://doi.org/10.1039/C7TA04122E
21. Ahmad I, Shukrullah S, Naz MY, Ahmad M, Ahmed E, Liu Y, Hussain A, Iqbal S, Ullah S (2022) Recent advances and challenges in 2D/2D heterojunction photocatalysts for solar fuels applications. Adv Coll Interface Sci 304:102661. https://doi.org/10.1016/j.cis.2022.102661
22. Scheff SW (2016) Chapter 8—nonparametric statistics. In: Scheff SW (ed) Fundamental statistical principles for the neurobiologist. Academic Press, London, pp 157–182. https://doi.org/10.1016/B978-0-12-804753-8.00008-7
23. Bao F, Kemppainen E, Dorbandt I, Bors R, Xi F, Schlatmann R, van de Krol R, Calnan S (2021) Understanding the hydrogen evolution reaction kinetics of electrodeposited nickel-molybdenum in acidic, near-neutral, and alkaline conditions. ChemElectroChem 8(1):195–208. https://doi.org/10.1002/celc.202001436
24. An X, Wang W, Wang J, Duan H, Shi J, Yu X (2018) The synergetic effects of Ti_3C_2 MXene and Pt as co-catalysts for highly efficient photocatalytic hydrogen evolution over g-C_3N_4. Phys Chem Chem Phys 20(16):11405–11411. https://doi.org/10.1039/C8CP01123K
25. Sun Y, Jin D, Sun Y, Meng X, Gao Y, Dall'Agnese Y, Chen G, Wang X-F, (2018) g-C_3N_4/$Ti_3C_2T_x$ (MXenes) composite with oxidized surface groups for efficient photocatalytic hydrogen evolution. J Mater Chem A 6(19):9124–9131. https://doi.org/10.1039/C8TA02706D
26. Zhang M, Qin J, Rajendran S, Zhang X, Liu R (2018) Heterostructured d-Ti_3C_2/TiO_2/g-C_3N_4 nanocomposites with enhanced visible-light photocatalytic hydrogen production activity. Chemsuschem 11(24):4226–4236. https://doi.org/10.1002/cssc.201802284
27. He K, Xie J, Liu Z-Q, Li N, Chen X, Hu J, Li X (2018) Multifunctional Ni_3C cocatalyst/g-C_3N_4 nanoheterojunctions for robust photocatalytic H_2 evolution under visible light. J Mater Chem A 6(27):13110–13122. https://doi.org/10.1039/C8TA03048K
28. Li Y, Ding L, Guo Y, Liang Z, Cui H, Tian J (2019) Boosting the photocatalytic ability of g-C_3N_4 for hydrogen production by Ti_3C_2 MXene quantum dots. ACS Appl Mater Interfaces 11(44):41440–41447. https://doi.org/10.1021/acsami.9b14985
29. Lin P, Shen J, Yu X, Liu Q, Li D, Tang H (2019) Construction of Ti_3C_2 MXene/O-doped g-C_3N_4 2D–2D Schottky-junction for enhanced photocatalytic hydrogen evolution. Ceram Int 45(18, Part A):24656–24663. https://doi.org/10.1016/j.ceramint.2019.08.203
30. Su T, Hood ZD, Naguib M, Bai L, Luo S, Rouleau CM, Ivanov IN, Ji H, Qin Z, Wu Z (2019) 2D/2D heterojunction of Ti_3C_2/g-C_3N_4 nanosheets for enhanced photocatalytic hydrogen evolution. Nanoscale 11(17):8138–8149. https://doi.org/10.1039/C9NR00168A
31. Xu F, Zhang D, Liao Y, Wang G, Shi X, Zhang H, Xiang Q (2020) Synthesis and photocatalytic H_2-production activity of plasma-treated $Ti_3C_2T_x$ MXene modified graphitic carbon nitride. J Am Ceram Soc 103(2):849–858. https://doi.org/10.1111/jace.16798
32. Han X, An L, Hu Y, Li Y, Hou C, Wang H, Zhang Q (2020) Ti_3C_2 MXene-derived carbon-doped TiO_2 coupled with g-C_3N_4 as the visible-light photocatalysts for photocatalytic H_2 generation. Appl Catal B 265:118539. https://doi.org/10.1016/j.apcatb.2019.118539
33. Zhang J, Wu M, He B, Wang R, Wang H, Gong Y (2019) Facile synthesis of rod-like g-C_3N_4 by decorating Mo_2C co-catalyst for enhanced visible-light photocatalytic activity. Appl Surf Sci 470:565–572. https://doi.org/10.1016/j.apsusc.2018.11.165
34. Kang J, Byun S, Kim S, Lee J, Jung M, Hwang H, Kim TW, Song SH, Lee D (2020) Design of three-dimensional

hollow-sphere architecture of $Ti_3C_2T_x$ MXene with graphitic carbon nitride nanoshells for efficient photocatalytic hydrogen evolution. ACS Appl Energy Mater 3(9):9226–9233. https://doi.org/10.1021/acsaem.0c01590
35. Li J, Zhao L, Wang S, Li J, Wang G, Wang J (2020) In situ fabrication of 2D/3D g-C_3N_4/Ti_3C_2 (MXene) heterojunction for efficient visible-light photocatalytic hydrogen evolution. Appl Surf Sci 515:145922. https://doi.org/10.1016/j.apsusc.2020.145922
36. Dong H, Zhang X, Zuo Y, Song N, Xin X, Zheng B, Sun J, Chen G, Li C (2020) 2D Ti_3C_2 as electron harvester anchors on 2D g-C_3N_4 to create boundary edge active sites for boosting photocatalytic performance. Appl Catal A 590:117367. https://doi.org/10.1016/j.apcata.2019.117367
37. Wu K, Song S, Wu H, Guo J, Zhang L (2020) Facile synthesis of Bi_2WO_6/C_3N_4/Ti_3C_2 composite as Z-scheme photocatalyst for efficient ciprofloxacin degradation and H_2 production. Appl Catal A 608:117869. https://doi.org/10.1016/j.apcata.2020.117869
38. Li J, Li J, Wu C, Li Z, Cai L, Tang H, Zhou Z, Wang G, Wang J, Zhao L, Wang S (2021) Crystalline carbon nitride anchored on MXene as an ordered Schottky heterojunction photocatalyst for enhanced visible-light hydrogen evolution. Carbon 179:387–399. https://doi.org/10.1016/j.carbon.2021.04.046
39. Song T, Hou L, Long B, Ali A, Deng G-J (2021) Ultrathin MXene "bridge" to accelerate charge transfer in ultrathin metal-free 0D/2D black phosphorus/g-C_3N_4 heterojunction toward photocatalytic hydrogen production. J Colloid Interface Sci 584:474–483. https://doi.org/10.1016/j.jcis.2020.09.103
40. Xu H, Xiao R, Huang J, Jiang Y, Zhao C, Yang X (2021) In situ construction of protonated g-C_3N_4/Ti_3C_2 MXene Schottky heterojunctions for efficient photocatalytic hydrogen production. Chin J Catal 42(1):107–114. https://doi.org/10.1016/S1872-2067(20)63559-8
41. Hieu VQ, Lam TC, Khan A, Thi Vo T-T, Nguyen T-Q, Doan VD, Tran DL, Le VT, Tran VA (2021) TiO_2/Ti_3C_2/g-C_3N_4 ternary heterojunction for photocatalytic hydrogen evolution. Chemosphere 285:131429. https://doi.org/10.1016/j.chemosphere.2021.131429
42. Liu W, Zhang D, Wang R, Zhang Z, Qiu S (2022) 2D/2D interface engineering promotes charge separation of Mo_2C/g-C_3N_4 nanojunction photocatalysts for efficient photocatalytic hydrogen evolution. ACS Appl Mater Interfaces 14(28):31782–31791. https://doi.org/10.1021/acsami.2c03421
43. Liu D, Li C, Ge J, Zhao C, Zhao Q, Zhang F, Ni T, Wu W (2022) 3D interconnected g-C_3N_4 hybridized with 2D Ti_3C_2 MXene nanosheets for enhancing visible light photocatalytic hydrogen evolution and dye contaminant elimination. Appl Surf Sci 579:152180. https://doi.org/10.1016/j.apsusc.2021.152180
44. Huang K, Lv C, Li C, Bai H, Meng X (2023) Ti_3C_2 MXene supporting platinum nanoparticles as rapid electrons transfer channel and active sites for boosted photocatalytic water splitting over g-C_3N_4. J Colloid Interface Sci 636:21–32. https://doi.org/10.1016/j.jcis.2022.12.169
45. Huang K, Li C, Zhang X, Wang L, Wang W, Meng X (2023) Self-assembly synthesis of phosphorus-doped tubular g-C_3N_4/Ti_3C_2 MXene Schottky junction for boosting photocatalytic hydrogen evolution. Green Energy Environ 8(1):233–245. https://doi.org/10.1016/j.gee.2021.03.011
46. fiqar Z, Tao J, Yang T, Liu Q, Hu J, Tang H, (2021) Designing 0D/2D CdS nanoparticles/g-C_3N_4 nanosheets heterojunction as efficient photocatalyst for improved H_2-evolution. Surf Interfaces 26:101312. https://doi.org/10.1016/j.surfin.2021.101312
47. Zhang S, Guo J, Zhang W, Gao H, Huang J, Chen G, Xu X (2021) Dopant and defect doubly modified CeO_2/g-C_3N_4 nanosheets as 0D/2D Z-Scheme heterojunctions for photocatalytic hydrogen evolution: experimental and density functional theory studies. ACS Sustain Chem Eng 9(34):11479–11492. https://doi.org/10.1021/acssuschemeng.1c03683
48. Zhu Y, Wan T, Wen X, Chu D, Jiang Y (2019) Tunable Type I and II heterojunction of CoO_x nanoparticles confined in g-C_3N_4 nanotubes for photocatalytic hydrogen production. Appl Catal B 244:814–822. https://doi.org/10.1016/j.apcatb.2018.12.015
49. Shi W, Li M, Huang X, Ren H, Yan C, Guo F (2020) Facile synthesis of 2D/2D $Co_3(PO_4)_2$/g-C_3N_4 heterojunction for highly photocatalytic overall water splitting under visible light. Chem Eng J 382:122960. https://doi.org/10.1016/j.cej.2019.122960
50. She X, Wu J, Xu H, Zhong J, Wang Y, Song Y, Nie K, Liu Y, Yang Y, Rodrigues M-TF, Vajtai R, Lou J, Du D, Li H, Ajayan PM (2017) High efficiency photocatalytic water splitting using 2D α-Fe_2O_3/g-C_3N_4 Z-scheme catalysts. Adv Energy Mater 7(17):1700025. https://doi.org/10.1002/aenm.201700025
51. Zhou X, Fang Y, Cai X, Zhang S, Yang S, Wang H, Zhong X, Fang Y (2020) In situ photodeposited construction of Pt–CdS/g-C_3N_4–MnO_x composite photocatalyst for efficient visible-light-driven overall water splitting. ACS Appl Mater Interfaces 12(18):20579–20588. https://doi.org/10.1021/acsami.0c04241
52. Tian N, Zhang Y, Li X, Xiao K, Du X, Dong F, Waterhouse GIN, Zhang T, Huang H (2017) Precursor-reforming protocol to 3D mesoporous g-C_3N_4 established by ultrathin self-doped nanosheets for superior hydrogen evolution. Nano Energy 38:72–81. https://doi.org/10.1016/j.nanoen.2017.05.038
53. Kong C, Zhang F, Sun X, Kai C, Cai W (2020) In-situ grown rod-shaped $Ni(OH)_2$ between interlayer of g-C_3N_4 for hydrogen evolution under visible light. Inorg Chem Commun 122:108264. https://doi.org/10.1016/j.inoche.2020.108264
54. Wang M, Huang S, Pang X, Song M, Du C, Su Y (2019) Switching charge kinetics from type-I to Z-scheme for g-C_3N_4 and $ZnIn_2S_4$ by defective engineering for efficient and durable hydrogen evolution. Sustain Energy Fuels 3(12):3422–3429. https://doi.org/10.1039/C9SE00639G
55. Bi Z-x, Guo R-t, Ji X-y, Hu X, Wang J, Chen X, Pan W-g (2022) Direct Z-scheme CoS/g-C_3N_4 heterojunction with NiS co-catalyst for efficient photocatalytic hydrogen generation. Int J Hydrogen Energy 47(81):34430–34443. https://doi.org/10.1016/j.ijhydene.2022.08.028
56. Liang Z, Xue Y, Guo Y, Zhang G, Cui H, Tian J (2020) Rationalizing and controlling the phase transformation of semi-metallic 1T′-phase and semi-conductive 2H-phase MoS_2 as cocatalysts for photocatalytic hydrogen evolution. Chem Eng J 396:125344. https://doi.org/10.1016/j.cej.2020.125344
57. Lin X, Du S, Li C, Li G, Li Y, Chen F, Fang P (2020) Consciously constructing the robust NiS/g-C_3N_4 hybrids for enhanced photocatalytic hydrogen evolution. Catal Lett 150(7):1898–1908. https://doi.org/10.1007/s10562-020-03118-x
58. Meng S, An P, Chen L, Sun S, Xie Z, Chen M, Jiang D (2021) Integrating Ru-modulated CoP nanosheets binary co-catalyst with 2D g-C_3N_4 nanosheets for enhanced photocatalytic hydrogen evolution activity. J Colloid Interface Sci 585:108–117. https://doi.org/10.1016/j.jcis.2020.11.066
59. Zheng Y, Dong J, Huang C, Xia L, Wu Q, Xu Q, Yao W (2020) Co-doped Mo-Mo_2C cocatalyst for enhanced g-C_3N_4 photocatalytic H_2 evolution. Appl Catal B 260:118220. https://doi.org/10.1016/j.apcatb.2019.118220
60. Su N, Cheng S, Zhang P, Dong H, Fang Y, Zhou X, Wang Y, Li C (2022) High-efficiency charge separation of Z-scheme 2D/2D C_3N_4/C_3N_5 nonmetal VdW heterojunction photocatalyst with enhanced hydrogen evolution activity and stability. Int J Hydrogen Energy 47(97):41010–41020. https://doi.org/10.1016/j.ijhydene.2022.09.188
61. Al-Ekabi H, Serpone N (1988) Kinetics studies in heterogeneous photocatalysis. I. Photocatalytic degradation of chlorinated phenols in aerated aqueous solutions over titania supported on

a glass matrix. J Phys Chem 92(20):5726–5731. https://doi.org/10.1021/j100331a036
62. Ding X, Li C, Wang L, Feng L, Han D, Wang W (2019) Fabrication of hierarchical g-C_3N_4/MXene-AgNPs nanocomposites with enhanced photocatalytic performances. Mater Lett 247:174–177. https://doi.org/10.1016/j.matlet.2019.02.125
63. Liu N, Lu N, Su Y, Wang P, Quan X (2019) Fabrication of g-C_3N_4/Ti_3C_2 composite and its visible-light photocatalytic capability for ciprofloxacin degradation. Sep Purif Technol 211:782–789. https://doi.org/10.1016/j.seppur.2018.10.027
64. Ding X, Li Y, Li C, Wang W, Wang L, Feng L, Han D (2019) 2D visible-light-driven TiO_2@Ti_3C_2/g-C_3N_4 ternary heterostructure for high photocatalytic activity. J Mater Sci 54(13):9385–9396. https://doi.org/10.1007/s10853-018-03289-4
65. Diao Y, Yan M, Li X, Zhou C, Peng B, Chen H, Zhang H (2020) In-situ grown of g-C_3N_4/Ti_3C_2/TiO_2 nanotube arrays on Ti meshes for efficient degradation of organic pollutants under visible light irradiation. Colloids Surf A 594:124511. https://doi.org/10.1016/j.colsurfa.2020.124511
66. He J, Yang J, Jiang F, Liu P, Zhu M (2020) Photo-assisted peroxymonosulfate activation via 2D/2D heterostructure of Ti_3C_2/g-C_3N_4 for degradation of diclofenac. Chemosphere 258:127339. https://doi.org/10.1016/j.chemosphere.2020.127339
67. Luo M, Feng H, Hu Y, Chen K, Dong Z, Xue S (2023) Visible light induced g-C_3N_4/TiO_2/Ti_3C_2 ternary Z-scheme heterojunction photocatalyst for efficient degradation. Electron Mater Lett 19(1):94–107. https://doi.org/10.1007/s13391-022-00377-1
68. Li B, Song H, Han F, Wei L (2020) Photocatalytic oxidative desulfurization and denitrogenation for fuels in ambient air over Ti_3C_2/g-C_3N_4 composites under visible light irradiation. Appl Catal B 269:118845. https://doi.org/10.1016/j.apcatb.2020.118845
69. Liu N, Lu N, Yu H, Chen S, Quan X (2020) Efficient day-night photocatalysis performance of 2D/2D Ti_3C_2/porous g-C_3N_4 nanolayers composite and its application in the degradation of organic pollutants. Chemosphere 246:125760. https://doi.org/10.1016/j.chemosphere.2019.125760
70. Vigneshwaran S, Karthikeyan P, Park CM, Meenakshi S (2020) Boosted insights of novel accordion-like (2D/2D) hybrid photocatalyst for the removal of cationic dyes: mechanistic and degradation pathways. J Environ Manag 273:111125. https://doi.org/10.1016/j.jenvman.2020.111125
71. Yi X, Yuan J, Tang H, Du Y, Hassan B, Yin K, Chen Y, Liu X (2020) Embedding few-layer $Ti_3C_2T_x$ into alkalized g-C_3N_4 nanosheets for efficient photocatalytic degradation. J Colloid Interface Sci 571:297–306. https://doi.org/10.1016/j.jcis.2020.03.061
72. Cao Z, Su J, Li Y, Li J, Wang Z, Li M, Fan B, Shao G, Wang H, Xu H, Zhang R, Lu H (2021) High-energy ball milling assisted one-step preparation of g-C_3N_4/TiO_2@Ti_3C_2 composites for effective visible light degradation of pollutants. J Alloys Compd 889:161771. https://doi.org/10.1016/j.jallcom.2021.161771
73. Yu M, Liang H, Zhan R, Xu L, Niu J (2021) Sm-doped g-C_3N_4/Ti_3C_2 MXene heterojunction for visible-light photocatalytic degradation of ciprofloxacin. Chin Chem Lett 32(7):2155–2158. https://doi.org/10.1016/j.cclet.2020.11.069
74. Liu W, Sun M, Ding Z, Gao B, Ding W (2021) Ti_3C_2 MXene embellished g-C_3N_4 nanosheets for improving photocatalytic redox capacity. J Alloys Compd 877:160223. https://doi.org/10.1016/j.jallcom.2021.160223
75. Tang R, Gong D, Deng Y, Xiong S, Deng J, Li L, Zhou Z, Zheng J, Su L, Yang L (2022) π-π Stacked step-scheme PDI/g-C_3N_4/TiO_2@Ti_3C_2 photocatalyst with enhanced visible photocatalytic degradation towards atrazine via peroxymonosulfate activation. Chem Eng J 427:131809. https://doi.org/10.1016/j.cej.2021.131809
76. Wu Z, Liang Y, Yuan X, Zou D, Fang J, Jiang L, Zhang J, Yang H, Xiao Z (2020) MXene Ti_3C_2 derived Z–scheme photocatalyst of graphene layers anchored TiO_2/g–C_3N_4 for visible light photocatalytic degradation of refractory organic pollutants. Chem Eng J 394:124921. https://doi.org/10.1016/j.cej.2020.124921
77. Zeng G, He Z, Wan T, Wang T, Yang Z, Liu Y, Lin Q, Wang Y, Sengupta A, Pu S (2022) A self-cleaning photocatalytic composite membrane based on g-C_3N_4@MXene nanosheets for the removal of dyes and antibiotics from wastewater. Sep Purif Technol 292:121037. https://doi.org/10.1016/j.seppur.2022.121037
78. Zu W, Jiang C, Liu W, Hou Q, Ji X (2022) Fabrication of a carbonized cellulose nanofibrils/$Ti_3C_2T_x$ MXene/g-C_3N_4 heterojunction for visible-light-driven photocatalysis. Langmuir 38(43):13109–13120. https://doi.org/10.1021/acs.langmuir.2c01818
79. Tu W, Liu Y, Chen M, Zhou Y, Xie Z, Ma L, Li L, Yang B (2022) Carbon nitride coupled with Ti_3C_2-Mxene derived amorphous Ti-peroxo heterojunction for photocatalytic degradation of rhodamine B and tetracycline. Colloids Surf A 640:128448. https://doi.org/10.1016/j.colsurfa.2022.128448
80. Zhou Y, Zhang C, Huang D, Wang W, Zhai Y, Liang Q, Yang Y, Tian S, Luo H, Qin D (2022) Structure defined 2D Mo_2C/2D g-C_3N_4 Van der Waals heterojunction: oriented charge flow in-plane and separation within the interface to collectively promote photocatalytic degradation of pharmaceutical and personal care products. Appl Catal B 301:120749. https://doi.org/10.1016/j.apcatb.2021.120749
81. Nasri MSI, Samsudin MFR, Tahir AA, Sufian S (2022) Effect of MXene loaded on g-C_3N_4 photocatalyst for the photocatalytic degradation of methylene blue. Energies 15(3):955
82. Gao K, Hou L-a, An X, Huang D, Yang Y (2023) BiOBr/MXene/gC_3N_4 Z-scheme heterostructure photocatalysts mediated by oxygen vacancies and MXene quantum dots for tetracycline degradation: process, mechanism and toxicity analysis. Appl Catal B 323:122150. https://doi.org/10.1016/j.apcatb.2022.122150
83. Hou Q, Wang M, Li T, Hou Y, Xuan K, Hao Y (2023) Peroxymonosulfate-assisted photocatalysis by a novel Ti_3C_2-based heterojunction catalyst (g-C_3N_4/Ti_3C_2/$MnFe_2O_4$) for enhanced degradation of naphthalene. Chem Eng J 464:142566. https://doi.org/10.1016/j.cej.2023.142566
84. Zhao Y, Que M, Chen J, Yang C (2020) MXenes as co-catalysts for the solar-driven photocatalytic reduction of CO_2. J Mater Chem C 8(46):16258–16281. https://doi.org/10.1039/D0TC02979C
85. He F, Zhu B, Cheng B, Yu J, Ho W, Macyk W (2020) 2D/2D/0D TiO_2/C_3N_4/Ti_3C_2 MXene composite S-scheme photocatalyst with enhanced CO_2 reduction activity. Appl Catal B 272:119006. https://doi.org/10.1016/j.apcatb.2020.119006
86. Tahir M, Tahir B (2020) 2D/2D/2D O-C_3N_4/Bt/$Ti_3C_2T_x$ heterojunction with novel MXene/clay multi-electron mediator for stimulating photo-induced CO_2 reforming to CO and CH_4. Chem Eng J 400:125868. https://doi.org/10.1016/j.cej.2020.125868
87. Tang Q, Sun Z, Deng S, Wang H, Wu Z (2020) Decorating g-C_3N_4 with alkalinized Ti_3C_2 MXene for promoted photocatalytic CO_2 reduction performance. J Colloid Interface Sci 564:406–417. https://doi.org/10.1016/j.jcis.2019.12.091
88. Yang C, Tan Q, Li Q, Zhou J, Fan J, Li B, Sun J, Lv K (2020) 2D/2D Ti_3C_2 MXene/g-C_3N_4 nanosheets heterojunction for high efficient CO_2 reduction photocatalyst: dual effects of urea. Appl Catal B 268:118738. https://doi.org/10.1016/j.apcatb.2020.118738
89. Hu J, Ding J, Zhong Q (2021) Ultrathin 2D Ti_3C_2 MXene Co-catalyst anchored on porous g-C_3N_4 for enhanced photocatalytic CO_2 reduction under visible-light irradiation. J Colloid Interface Sci 582:647–657. https://doi.org/10.1016/j.jcis.2020.08.047

90. Yang Y, Zhang D, Fan J, Liao Y, Xiang Q (2021) Construction of an ultrathin S-scheme heterojunction based on few-layer g-C_3N_4 and monolayer $Ti_3C_2T_x$ MXene for photocatalytic CO2 reduction. Solar RRL 5(2):2000351. https://doi.org/10.1002/solr.202000351
91. Wang H, Tang Q, Wu Z (2021) Construction of few-layer Ti_3C_2 MXene and boron-doped g-C_3N_4 for enhanced photocatalytic CO_2 reduction. ACS Sustain Chem Eng 9(25):8425–8434. https://doi.org/10.1021/acssuschemeng.1c01155
92. Khan AA, Tahir M (2021) Well-designed 2D/2D $Ti_3C_2T_{A/R}$ MXene coupled g-C_3N_4 heterojunction with in-situ growth of anatase/rutile TiO_2 nucleates to boost photocatalytic dry-reforming of methane (DRM) for syngas production under visible light. Appl Catal B 285:119777. https://doi.org/10.1016/j.apcatb.2020.119777
93. Li X, Bai Y, Shi X, Huang J, Zhang K, Wang R, Ye L (2021) Mesoporous g-C_3N_4/MXene ($Ti_3C_2T_x$) heterojunction as a 2D electronic charge transfer for efficient photocatalytic CO_2 reduction. Appl Surf Sci 546:149111. https://doi.org/10.1016/j.apsusc.2021.149111
94. Hong L-f, Guo R-t, Yuan Y, Ji X-y, Lin Z-d, Yin X-f, Pan W-g (2022) 2D Ti_3C_2 decorated Z-scheme $BiOIO_3$/g-C_3N_4 heterojunction for the enhanced photocatalytic CO_2 reduction activity under visible light. Colloids Surf A 639:128358. https://doi.org/10.1016/j.colsurfa.2022.128358
95. Madi M, Tahir M, Zakaria ZY (2022) 2D/2D V_2C mediated porous g-C_3N_4 heterojunction with the role of monolayer/multilayer MAX/MXene structures for stimulating photocatalytic CO_2 reduction to fuels. J CO2 Util 65:102238. https://doi.org/10.1016/j.jcou.2022.102238
96. Song Q, Hu J, Zhou Y, Ye Q, Shi X, Li D, Jiang D (2022) Carbon vacancy-mediated exciton dissociation in Ti_3C_2Tx/g-C_3N_4 Schottky junctions for efficient photoreduction of CO_2. J Colloid Interface Sci 623:487–499. https://doi.org/10.1016/j.jcis.2022.05.064
97. Li J, Wang Y, Wang Y, Guo Y, Zhang S, Song H, Li X, Gao Q, Shang W, Hu S, Zheng H, Li X (2023) MXene Ti_3C_2 decorated g-C_3N_4/ZnO photocatalysts with improved photocatalytic performance for CO_2 reduction. Nano Mater Sci. https://doi.org/10.1016/j.nanoms.2023.02.003
98. Qin H, Guo R-T, Liu X-Y, Shi X, Wang Z-Y, Tang J-Y, Pan W-G (2020) 0D NiS_2 quantum dots modified 2D g-C_3N_4 for efficient photocatalytic CO_2 reduction. Colloids Surf A 600:124912. https://doi.org/10.1016/j.colsurfa.2020.124912
99. Sun Z, Wang H, Wu Z, Wang L (2018) g-C_3N_4 based composite photocatalysts for photocatalytic CO_2 reduction. Catal Today 300:160–172. https://doi.org/10.1016/j.cattod.2017.05.033
100. Ye L, Wu D, Chu KH, Wang B, Xie H, Yip HY, Wong PK (2016) Phosphorylation of g-C_3N_4 for enhanced photocatalytic CO_2 reduction. Chem Eng J 304:376–383. https://doi.org/10.1016/j.cej.2016.06.059
101. Tang J-y, Guo R-t, Pan W-g, Zhou W-g, Huang C-y (2019) Visible light activated photocatalytic behaviour of Eu(III) modified g-C_3N_4 for CO_2 reduction and H_2 evolution. Appl Surf Sci 467–468:206–212. https://doi.org/10.1016/j.apsusc.2018.10.143
102. Han X, Li M, Ma Y, Li Y, Ma H, Wang C (2021) Thermal coupled photocatalysis to enhance CO_2 reduction activities on Ag loaded g-C_3N_4 catalysts. Surf Interfaces 23:101006. https://doi.org/10.1016/j.surfin.2021.101006
103. Tang Z, Wang C, He W, Wei Y, Zhao Z, Liu J (2022) The Z-scheme g-C_3N_4/3DOM-WO_3 photocatalysts with enhanced activity for CO_2 photoreduction into CO. Chin Chem Lett 33(2):939–942. https://doi.org/10.1016/j.cclet.2021.07.020
104. Wang C, Zhao Y, Xu H, Li Y, Wei Y, Liu J, Zhao Z (2020) Efficient Z-scheme photocatalysts of ultrathin g-C_3N_4-wrapped Au/TiO_2-nanocrystals for enhanced visible-light-driven conversion of CO_2 with H_2O. Appl Catal B 263:118314. https://doi.org/10.1016/j.apcatb.2019.118314
105. Zhou D, Zhang J, Jin Z, Di T, Wang T (2022) Reduced graphene oxide assisted g-C_3N_4/rGO/NiAl-LDHs type II heterostructure with high performance photocatalytic CO_2 reduction. Chem Eng J 450:138108. https://doi.org/10.1016/j.cej.2022.138108
106. Wang C, Liu X, He W, Zhao Y, Wei Y, Xiong J, Liu J, Li J, Song W, Zhang X, Zhao Z (2020) All-solid-state Z-scheme photocatalysts of g-C_3N_4/Pt/macroporous-(TiO_2@carbon) for selective boosting visible-light-driven conversion of CO_2 to CH_4. J Catal 389:440–449. https://doi.org/10.1016/j.jcat.2020.06.026
107. Zhao X, Han D, Dai M, Fan Y, Wang Z, Han D, Niu L (2022) Direct Z-scheme FeV_2O_4/g-C_3N_4 binary catalyst for highly selective reduction of carbon dioxide. Chem Eng J 436:132051. https://doi.org/10.1016/j.cej.2021.132051
108. Jia X, Sun H, Lin H, Cao J, Hu C, Chen S (2023) In-depth insight into the mechanism on photocatalytic selective CO_2 reduction coupled with tetracycline oxidation over $BiO_{1-x}Br$/g-C_3N_4. Appl Surf Sci 614:156017. https://doi.org/10.1016/j.apsusc.2022.156017
109. Qaraah FA, Mahyoub SA, Hezam A, Qaraah A, Xin F, Xiu G (2022) Synergistic effect of hierarchical structure and S-scheme heterojunction over O-doped g-C_3N_4/N-doped Nb_2O_5 for highly efficient photocatalytic CO_2 reduction. Appl Catal B 315:121585. https://doi.org/10.1016/j.apcatb.2022.121585
110. Xu Y, Jin X, Ge T, Xie H, Sun R, Su F, Li X, Ye L (2021) Realizing efficient CO_2 photoreduction in Bi_3O_4Cl: constructing van der Waals heterostructure with g-C_3N_4. Chem Eng J 409:128178. https://doi.org/10.1016/j.cej.2020.128178
111. He W, Wei Y, Xiong J, Tang Z, Wang Y, Wang X, Deng J, Yu X, Zhang X, Zhao Z (2022) Boosting selective photocatalytic CO_2 reduction to CO over Dual-core@shell structured Bi_2O_3/Bi_2WO_6@g-C_3N_4 catalysts with strong interaction interface. Sep Purif Technol 300:121850. https://doi.org/10.1016/j.seppur.2022.121850
112. Guo R-t, Liu X-y, Qin H, Wang Z-y, Shi X, Pan W-g, Fu Z-g, Tang J-y, Jia P-y, Miao Y-f, Gu J-w (2020) Photocatalytic reduction of CO_2 into CO over nanostructure Bi_2S_3 quantum dots/g-C_3N_4 composites with Z-scheme mechanism. Appl Surf Sci 500:144059. https://doi.org/10.1016/j.apsusc.2019.144059
113. Wu J, Huang Y, Ye W, Li Y (2017) CO_2 reduction: from the electrochemical to photochemical approach. Adv Sci 4(11):1700194. https://doi.org/10.1002/advs.201700194
114. Morales-Salvador R, Gouveia JD, Morales-García Á, Viñes F, Gomes JRB, Illas F (2021) Carbon capture and usage by MXenes. ACS Catal 11(17):11248–11255. https://doi.org/10.1021/acscatal.1c02663
115. Liu Q, Ai L, Jiang J (2018) MXene-derived TiO_2@C/g-C_3N_4 heterojunctions for highly efficient nitrogen photofixation. J Mater Chem A 6(9):4102–4110. https://doi.org/10.1039/C7TA09350K
116. Jiang H, Zang C, Zhang Y, Wang W, Yang C, Sun B, Shen Y, Bian F (2020) 2D MXene-derived Nb_2O_5/C/Nb_2C/g-C_3N_4 heterojunctions for efficient nitrogen photofixation. Catal Sci Technol 10(17):5964–5972. https://doi.org/10.1039/D0CY00656D
117. Sun C, Chen Z, Cui J, Li K, Qu H, Xie H, Zhong Q (2021) Site-exposed Ti_3C_2 MXene anchored in N-defect g-C_3N_4 heterostructure nanosheets for efficient photocatalytic N_2 fixation. Catal Sci Technol 11(3):1027–1038. https://doi.org/10.1039/D0CY01955K
118. Chang B, Guo Y, Liu H, Li L, Yang B (2022) Engineering a surface defect-rich Ti_3C_2 quantum dots/mesoporous C_3N_4 hollow nanosphere Schottky junction for efficient N_2 photofixation. J Mater Chem A 10(6):3134–3145. https://doi.org/10.1039/D1TA09941H
119. Li J, Zhang Q, Zou Y, Cao Y, Cui W, Dong F, Zhou Y (2020) Ti_3C_2 MXene modified g-C_3N_4 with enhanced visible-light

photocatalytic performance for NO purification. J Colloid Interface Sci 575:443–451. https://doi.org/10.1016/j.jcis.2020.04.119
120. Zhang X, Nie J, Rao F, Liu H, Wang Y, Qu D, Wu W, Zhong P, Zhu G (2021) Ti_3C_2@TiO_2/g-C_3N_4 heterojunction photocatalyst with improved charge transfer for enhancing visible-light NO selective removal. Ceram Int 47(22):31302–31310. https://doi.org/10.1016/j.ceramint.2021.08.003
121. Wang T, Yang W, Chang L, Wang H, Wu H, Cao J, Fan H, Wang J, Liu H, Hou Y, Zhang R, Yang Z, Zhu H, Kong C (2022) One-step calcination synthesis of accordion-like MXene-derived TiO_2@C coupled with g-C_3N_4: Z-scheme heterojunction for enhanced photocatalytic NO removal. Sep Purif Technol 285:120329. https://doi.org/10.1016/j.seppur.2021.120329
122. Hu X, Wang Y, Ling Z, Song H, Cai Y, Li Z, Zu D, Li C (2021) Ternary g-C_3N_4/TiO_2/Ti_3C_2 MXene S-scheme heterojunction photocatalysts for NO_x removal under visible light. Appl Surf Sci 556:149817. https://doi.org/10.1016/j.apsusc.2021.149817
123. Wang T, Chang L, Wu H, Yang W, Cao J, Fan H, Wang J, Liu H, Hou Y, Jiang Y, Zhu H (2022) Fabrication of three-dimensional hierarchical porous 2D/0D/2D g-C_3N_4 modified MXene-derived TiO_2@C: synergy effect of photocatalysis and H_2O_2 oxidation in NO removal. J Colloid Interface Sci 612:434–444. https://doi.org/10.1016/j.jcis.2021.12.120
124. Yang Y, Zeng Z, Zeng G, Huang D, Xiao R, Zhang C, Zhou C, Xiong W, Wang W, Cheng M, Xue W, Guo H, Tang X, He D (2019) Ti_3C_2 Mxene/porous g-C_3N_4 interfacial Schottky junction for boosting spatial charge separation in photocatalytic H_2O_2 production. Appl Catal B 258:117956. https://doi.org/10.1016/j.apcatb.2019.117956
125. Lin S, Zhang N, Wang F, Lei J, Zhou L, Liu Y, Zhang J (2021) Carbon vacancy mediated incorporation of Ti_3C_2 quantum dots in a 3D inverse Opal g-C_3N_4 Schottky junction catalyst for photocatalytic H_2O_2 production. ACS Sustain Chem Eng 9(1):481–488. https://doi.org/10.1021/acssuschemeng.0c07753
126. Wang X-X, Meng S, Zhang S, Zheng X, Chen S (2020) 2D/2D MXene/g-C_3N_4 for photocatalytic selective oxidation of 5-hydroxymethylfurfural into 2,5-formylfuran. Catal Commun 147:106152. https://doi.org/10.1016/j.catcom.2020.106152
127. Zhou J, Li D, Zhao W, Jing B, Ao Z, An T (2021) First-principles evaluation of volatile organic compounds degradation in Z-scheme photocatalytic systems: MXene and graphitic-CN heterostructures. ACS Appl Mater Interfaces 13(20):23843–23852. https://doi.org/10.1021/acsami.1c05617
128. Li S, Wang Y, Wang J, Liang J, Li Y, Li P (2022) Modifying g-C_3N_4 with oxidized Ti_3C_2 MXene for boosting photocatalytic U(VI) reduction performance. J Mol Liq 346:117937. https://doi.org/10.1016/j.molliq.2021.117937
129. Makola LC, Moeno S, Ouma CNM, Sharma A, Vo D-VN, Dlamini LN (2022) Facile fabrication of a metal-free 2D–2D Nb_2CTx@g-C_3N_4 MXene-based Schottky-heterojunction with the potential application in photocatalytic processes. J Alloys Compd 916:165459. https://doi.org/10.1016/j.jallcom.2022.165459